

The chemical footprint of the star formation feedback in M 82 on scales of ~ 100 pc[★]

D. Ginard¹, A. Fuente¹, S. García-Burillo², T. Alonso-Albi², M. Krips³, M. Gerin⁴, R. Neri³, P. Pilleri^{5,6}, A. Usero², and S.P. Treviño-Morales⁷

¹ Observatorio Astronómico Nacional (OAN, IGN), Apdo. 112, E-28800 Alcalá de Henares, Madrid, Spain

² Observatorio Astronómico Nacional (OAN, IGN), Observatorio de Madrid, Alfonso XII, 3, E-28014, Madrid

³ Institut de Radioastronomie Millimétrique, 300 rue de la Piscine, F-38406 St Martin d'Hères, France

⁴ CNRS UMR8112, LERMA, Observatoire de Paris and Ecole Normale Supérieure, 24 Rue Lhomond, 75231 Paris cedex 05, France

⁵ Université de Toulouse; UPS-OMP; IRAP; Toulouse, France

⁶ CNRS; IRAP; 9 Av. colonel Roche, BP 44346, F-31028 Toulouse cedex 4, France

⁷ Instituto de Radioastronomía Milimétrica (IRAM-Spain), Ave. Divina Pastora, 7, E-18012 Granada, Spain

Received September , 2014; accepted December –, 2014

ABSTRACT

Context. M 82 is one of the nearest and brightest starburst galaxies. It has been extensively studied in the last decade and by now it is considered as the prototypical extragalactic PDR and a reference for the study of the star formation feedback.

Aims. Our aim is to characterize the molecular chemistry in M 82 at spatial scales of giant molecular clouds (GMCs), ~ 100 pc, to investigate the feedback effects of the star formation activity.

Methods. We present interferometric observations of the CN $1\rightarrow 0$ (113.491 GHz), N₂H⁺ $1\rightarrow 0$ (93.173 GHz), H(41) α (92.034 GHz), CH₃CN (91.987 GHz), CS $3\rightarrow 2$ (146.969 GHz), c-C₃H₂ $3_{1,2}\rightarrow 2_{2,1}$ (145.089 GHz), H₂CO $2_{0,2}\rightarrow 1_{0,1}$ (145.603 GHz) and HC₃N $16\rightarrow 15$ (145.601 GHz) lines carried out with the IRAM Plateau de Bure Interferometer (PdBI). PDR chemical modelling is used to interpret these observations.

Results. Our results show that the abundances of N₂H⁺, CS and H¹³CO⁺ remain quite constant across the galaxy confirming that these species are excellent tracers of the dense molecular gas. On the contrary, the abundance of CN increases by a factor of ~ 3 in the inner x_2 bar orbits. The [CN]/[N₂H⁺] ratio is well correlated with the H(41) α emission at all spatial scales down to ~ 100 pc. Chemical modelling shows that the variations in the [CN]/[N₂H⁺] ratio can be explained as the consequence of differences in the local interstellar UV field and in the average cloud sizes within the nucleus of the galaxy.

Conclusions. Our high-spatial resolution imaging of the starburst galaxy M 82 shows that the star formation activity has a strong impact on the chemistry of the molecular gas. In particular, the entire nucleus behaves as a giant photon-dominated region (PDR) whose chemistry is determined by the local UV flux. The detection of N₂H⁺ shows the existence of a population of clouds with $A_V > 20$ mag all across the galaxy plane. These clouds constitute the molecular gas reservoir for the formation of new stars and, although distributed all along the nucleus, the highest concentration occurs in the outer x_1 bar orbits ($R \sim 280$ pc).

Key words. Galaxies: Individual: Messier Number: M 82, Galaxies: Nuclei, Galaxies: Starburst, ISM: Molecules, Molecular Processes, Radio Lines: Galaxies

1. Introduction

M 82 is one of the nearest and brightest starburst galaxies. Located at a distance of 3.9 Mpc, and with a luminosity of $3.7 \times 10^{10} L_\odot$, it has been the subject of continuum and line observations at all wavelengths from X-rays to the radio domains. Several molecular line studies indicate that the strong UV field has heavily influenced the physical conditions, kinematics and chemistry of the interstellar gas (Mao et al. 2000; Weiss et al. 2001a,b; García-Burillo et al. 2001, 2002; Fuente et al. 2005, 2006, 2008; Aladro et al. 2011). In fact M 82 has become the prototypical extragalactic PDR and a reference for the study and interpretation of star formation feedback in extreme starbursts near and far.

The presence of a stellar bar in M 82 has been invoked as a mechanism to fuel the star formation activity in the inner $r \sim 30''$

(500 pc) disk of the galaxy. The stellar bar, studied in detail by Greve et al. (2002), could have formed during the encounter of M 81 and M 82. The orbits sustaining the bar potential, denoted as x_1 orbits, are oriented parallel to the bar major axis, and extend out to $r \sim 30''$ (500 pc) in the disk. The M 82's stellar bar seems to have room for x_2 orbits, which are oriented parallel to the bar minor axis, in the inner $r \sim 5''$ (~ 90 pc). Evidence supporting the existence of x_2 orbits in M 82 is derived from the position-velocity diagrams obtained in several tracers of the ISM, including CO, HI and [NeII] emission line data (Shen & Lo 1995; Neininger et al. 1998; Wills et al. 2000; Achtermann & Lacy 1995). Coupled stellar population synthesis and photoionization models reveal two major episodes of star formation over the past 10 Myr (Förster-Schreiber et al. 2003). The first episode (~ 10 Myr) took place throughout the central regions of M 82 and was particularly intense at the nucleus while the second episode (~ 5 Myr) occurred predominantly in a circumnuclear ring at a radius of ~ 90 pc and along the stellar bar. This inside-outside scenario can be understood as resulting from the gravitational

Based on observations carried out with the IRAM Plateau de Bure Interferometer. IRAM is supported by INSU/CNRS (France), MPG (Germany), and IGN (Spain).

Table 1. Observations

	Line	Freq. (GHz)	beam (")	Fields	T _b /Flux K/(Jy/beam)	Date or ref ¹
C ¹⁸ O	1→0	109.782	3.8"×3.5" PA -4°	(0", 0")	7.6	W01 (Zero-spacing)
CO	2→1	230.538	1.5"×1.4" PA 0°	(-30", -8"), (-20", -6") (-10", -4"), (10", 4") (20", 8"), (30", 10")	11	W01 (Zero-spacing)
CN	1→0	113.491	2.5"×2.3" PA 170°	(0", 0")	17	May-Dec 2005
H ¹³ CO ⁺	1→0	86.754	5.9"×5.6" PA 105°	(0", 0")	5	G01
HCO	1→0	86.670	5.9"×5.6" PA 105°	(0", 0")	5	G01
HOC ⁺	1→0	89.487	4.4"×3.6" PA 128°	(0", 0")	9	F08
N ₂ H ⁺	1→0	93.173	3.6"×2.7" PA 94°	(0", 0")	14	Dec 2010 - May 2011
H	(41) α	92.034	3.5"×2.8" PA 94°	(0", 0")	15	Dec 2010 - May 2011
CH ₃ CN	5 ₃ →4 ₀	91.971	3.5"×2.8" PA 94°	(0", 0")	15	Dec 2010 - May 2011
	5 ₂ →4 ₂	91.980	3.5"×2.8" PA 94°	(0", 0")	15	Dec 2010 - May 2011
	5 ₁ →4 ₁	91.985	3.5"×2.8" PA 94°	(0", 0")	15	Dec 2010 - May 2011
	5 ₀ →4 ₀	91.987	3.5"×2.8" PA 94°	(0", 0")	15	Dec 2010 - May 2011
H	(35) α	147.047	2.3"×1.9" PA 75°	(+7", +2.5"), (-7", -2.5")	13	Dec 2010 - May 2011
CS	3→2	146.969	2.3"×1.9" PA 75°	(+7", +2.5"), (-7", -2.5")	12	Dec 2010 - May 2011
c-C ₃ H ₂	3 _{1,2} →2 _{2,1}	145.089	2.3"×1.9" PA 75°	(+7", +2.5"), (-7", -2.5")	12	Dec 2010 - May 2011
A-CH ₃ OH	3 _{0,0} →2 _{0,0}	145.103	2.3"×1.9" PA 75°	(+7", +2.5"), (-7", -2.5")	12	Dec 2010 - May 2011
E-CH ₃ OH	3 _{0,0} →2 _{0,0}	145.094	2.3"×1.9" PA 75°	(+7", +2.5"), (-7", -2.5")	12	Dec 2010 - May 2011
	3 _{-1,0} →2 _{-1,0}	145.097	2.3"×1.9" PA 75°	(+7", +2.5"), (-7", -2.5")	12	Dec 2010 - May 2011
H ₂ CO	2 _{0,2} →1 _{0,1}	145.603	2.3"×1.9" PA 75°	(+7", +2.5"), (-7", -2.5")	12	Dec 2010 - May 2011
HC ₃ N	16→15	145.561	2.3"×1.9" PA 75°	(+7", +2.5"), (-7", -2.5")	12	Dec 2010 - May 2011

¹ W01: Weiss et al. (2001b); G01: García-Burillo et al. (2001); F08: Fuente et al. (2008)

interaction between M 82 and its neighbour M 81, and subsequent bar-driven evolution. Each episode lasted only for a few million years suggesting strong negative feedback effects from the starburst activity.

X-rays and optical observations have shown the existence of a biconical outflow of hot gas coming out of the plane in the nucleus of M 82 (Bregman et al. 1995, Shopbell et al. 1998). It is widely accepted that the driving mechanism of the outflow phenomenon in starbursts is linked to the creation of expanding shells of hot gas by supernovae. These hot bubbles blow out into the halo, entraining surrounding cold gas and dust at several hundreds of kilometers per second. Interferometric observations showed that, contrary to most species, the SiO emission is not tracing the molecular gas in the galaxy disk. The detection of a ~500 pc molecular gas chimney and a super-shell in SiO indicates the occurrence of large-scale shocks in the disk-halo interface (García-Burillo et al. 2001). Out-of-plane molecular emission has also been detected in CO, HCN and HCO⁺ (Weiss et al. 2001b, Salas et al. 2014). Recent observations of the HCN 1→0 and HCO⁺ 1→0 lines by Salas et al. (2014) showed that >2% of the total dense molecular gas is in the outflow formed by the gas expelled by the central starburst.

M 82 is one of the finest examples of how chemistry can help to the full understanding of the interstellar medium (ISM) of an external galaxy. Our early HCO interferometric map using the PdBI showed that the M 82 nucleus is a giant photon-dominated region (PDR) of ~650 pc size. Furthermore the comparison between the HCO and H¹³CO⁺ images suggested that the PDR chemistry is propagating across the M 82 nucleus. Our subsequent 30m and PdBI chemical studies provided further support for the existence of giant PDRs in the galaxy disk (García-Burillo et al. 2002, Fuente et al. 2005, 2006, 2008). In particular it is remarkable the detection of the reactive ion CO⁺ using the 30m telescope (Fuente et al. 2006), the first time in an external galaxy, and the interferometric image of the HOC⁺ 1→0

line (Fuente et al. 2008), the first one ever observed. Chemical modeling using the Meudon PDR code showed that most of the observations (CO⁺, HOC⁺, HCO⁺, CN, HCN, H₃O⁺) are well explained assuming that about 87% of the mass of the molecular gas is forming small (~0.02 pc) clouds with a total thickness of ~5 mag. In these small clouds all the molecular gas is exposed to an intense UV field and the entire cloud is a PDR. Further star formation is not expected in this PDR component. A small mass fraction (~13%) must, however, be located in shielded regions to account for the measured [CN]/[HCN] abundance ratio. We estimated that these clouds could have large column densities, with a total visual extinction of >50 mag. The existence of this shielded component is also necessary to explain the detection of some species like NH₃ and CH₃OH (Weiss et al. 2001a, Martín et al. 2006, Aladro et al. 2011).

However, this chemical study was based on single-dish 30m observations towards one position (position E in the nomenclature of Fuente et al. 2008) and cannot be extrapolated to the entire galaxy. In addition, all the observed molecules were PDR tracers which are not adequate to trace the shielded gas. In this paper, we present high spatial resolution (~100 pc) observations of a set of molecular lines carried out with the Plateau de Bure Interferometer (PdBI). This set of molecules includes PDR tracers like CN and c-C₃H₂ but also well-known tracers of cold and dense gas like N₂H⁺, CS and C¹⁸O. We combine the information from all these molecules to gain insights into the spatial distribution, physical conditions and chemistry of the molecular gas reservoir in the M 82 starburst.

2. Observations and data reduction

The interferometric observations of the CN 1→0 (113.491 GHz), N₂H⁺ 1→0 (93.173 GHz), CS 3→2 (146.969 GHz), c-C₃H₂ 3_{1,2}→2_{2,1} (145.089 GHz), H₂CO 2_{0,2}→1_{0,1} (145.603 GHz) and HC₃N 16→15 (145.601 GHz) lines were carried out with

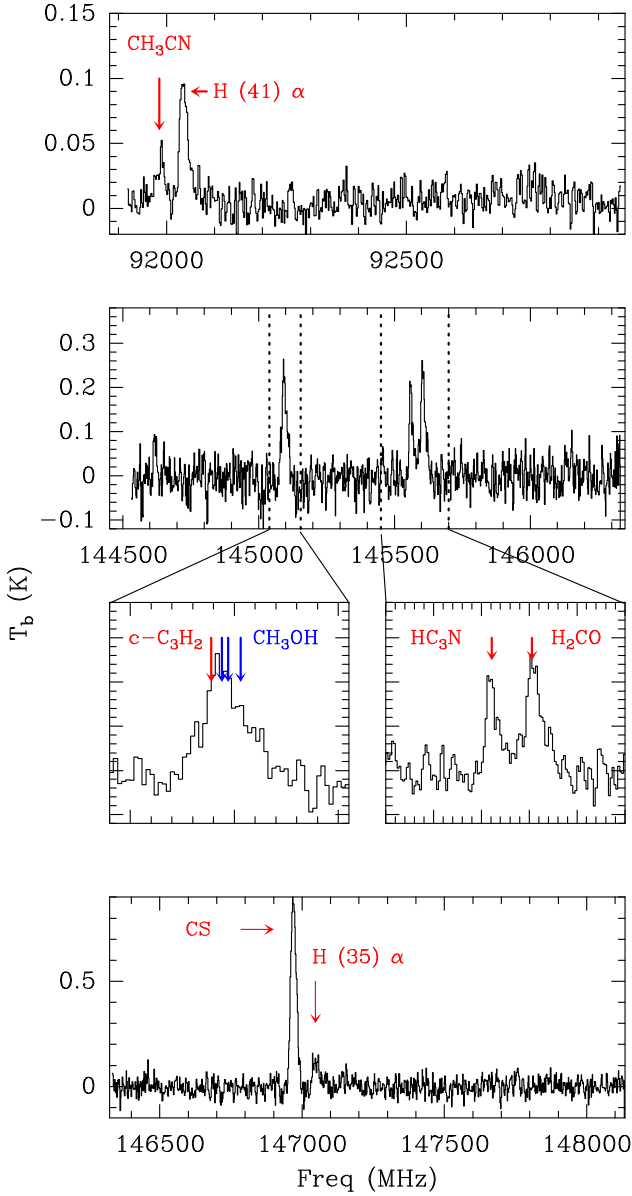


Fig. 1. Interferometric spectra towards E1 [offset (+14'', +5'')] in temperature units (K). The velocity has been set to $v_{lsr}=330$ km s $^{-1}$, based on the C 18 O data. Vertical lines indicate the following frequencies: 91987 (CH $_3$ CN $5_0 \rightarrow 4_0$), 92034 (H(41) α), 145561 (HC $_3$ N $16 \rightarrow 15$), 145603 (H $_2$ CO $2_{0,1} \rightarrow 1_{0,1}$), 145089 (c-C $_3$ H $_2$ $3_{1,2} \rightarrow 2_{2,1}$), 145094 (E-CH $_3$ OH $3_{0,0} \rightarrow 2_{0,0}$), 145097 (E-CH $_3$ OH $3_{-1,0} \rightarrow 2_{-1,0}$), 145103 (A-CH $_3$ OH $3_{0,0} \rightarrow 2_{0,0}$), 146969 (CS $3 \rightarrow 2$), and 147047 (H(35) α) MHz.

the IRAM Plateau de Bure Interferometer (PdBI) as part of two different projects. The CN $1 \rightarrow 0$ line was imaged in May and December, 2005, with the antennas arranged in the C and D configurations providing almost a circular beam of $2.46'' \times 2.27''$ PA 170° . The primary beam of the PdBI at this frequency is $\sim 44''$, enough to cover the whole galactic plane at 3mm and only one field was observed. During the observations we adjusted the spectral correlator to give a contiguous bandwidth of 1 GHz with a frequency resolution of 2.5 MHz. The continuum maps were generated using the channels free of line emission. Then we subtracted the continuum emission to produce the spectroscopic maps. The maps have been cor-

rected for the primary beam attenuation (primary beam= $44''$ at 113.5 GHz).

In the second project we imaged the N $_2$ H $^+$ $1 \rightarrow 0$ (93.173 MHz), CS $3 \rightarrow 2$ (146.969 MHz), c-C $_3$ H $_2$ $3_{1,2} \rightarrow 2_{2,1}$ (145.089 MHz), H $_2$ CO $2_{0,2} \rightarrow 1_{0,1}$ (145.603 MHz) and HC $_3$ N $16 \rightarrow 15$ (145.601 MHz) lines. These observations were carried out on December, 2010 and May, 2011, with the antennas arranged in the C configuration. During the 3mm observations, the narrow band correlators were placed to cover the N $_2$ H $^+$ $1 \rightarrow 0$ line with a frequency resolution of 20 kHz. We used the wide-band correlator WideX to cover a bandwidth of 3.6 GHz in dual polarization with a channel spacing of about 1.95 MHz. This allowed us to observe the H(41) α recombination line at 92.034 GHz and the CH $_3$ CN $5_k \rightarrow 4_k$ $k=0,1,2,3$ at ~ 91.987 GHz simultaneously with the N $_2$ H $^+$ $1 \rightarrow 0$ line (see Fig. 1). Only one field was observed and the maps have been corrected for primary beam attenuation (primary beam= $54''$ at 92.5 GHz). The synthesized beam was almost circular with HPBW $\sim 3.56'' \times 2.74''$ PA 94° . Because of the slightly better sensitivity, we used the WideX cube for our analysis.

At 2mm, we observed two fields at (+7'', +2.5'') and (-7'', -2.5''). The CS $3 \rightarrow 2$ line was covered with the narrow band correlators providing a frequency resolution of 160 kHz. The wide-band correlator WideX was used to cover a bandwidth of 3.6 GHz in dual polarization with a channel spacing of about 1.95 MHz. This allowed us to observe the H(35) α and the c-C $_3$ H $_2$ $3_{1,2} \rightarrow 2_{2,1}$, CH $_3$ OH $3 \rightarrow 2$, H $_2$ CO $2_{0,2} \rightarrow 1_{0,1}$ and HC $_3$ N $16 \rightarrow 15$ lines in the same setting. In Fig. 1 we present the observed spectrum towards the position (+14'', +5''). Unfortunately, the c-C $_3$ H $_2$ line is blended with several CH $_3$ OH $3 \rightarrow 2$ lines and cannot be separated (see Fig. 1). The H $_2$ CO $2_{0,2} \rightarrow 1_{0,1}$ (145.603 MHz) and HC $_3$ N $16 \rightarrow 15$ (145.601 MHz) lines are partially blended and cannot be imaged separately, but can be separated in the outer part of the galaxy where the linewidths are narrower. We generated continuum maps using the channels free of line emission to subtract the continuum from the spectral images. The HPBW of the synthesized beam is $\sim 2.3'' \times 1.88''$ PA 75° .

Data analysis and image processing have been done using the GILDAS package software (<http://www.iram.fr/IRAMFR/GILDAS/>) and JPARSEC (<http://conga.oan.es/~alonso/doku.php?id=jparsec>).

All the maps are centered at, RA = 09:55:51.9, Dec = +69:40:47.10 (J2000), that is the 2.2μ m peak as determined by Joy, Lester & Harvey (1987). This is also the central position used in previous interferometric studies (Weiss et al. 2001b, García-Burillo et al. 2001, 2002, Fuente et al. 2008). Lester et al. (1990) established the 2μ m peak at RA = 09:55:52.4, Dec = +69:40:46.00 (J2000), i.e. +2.7'' E 1.3'' S from our center position. The M 82 galactic plane is viewed almost edge-on ($i \sim 80^\circ$, Greve 2011). In order to guide the discussion, we have defined four positions E1, E2, W2, and W1 [(+14'', +5''), (+5'', +2''), (-5'', -2'') and (-14'', -5''), respectively] that are aligned with the center at an angle of 68° . Within the errors, this is the position angle of the galactic plane. The intense continuum source SN 41.9+58 is located (-1.25'', -1.1'') from our position W2 (Kronberg et al. 1981, Weiss et al. 1999). Position E1 coincides with position E in Fuente et al. (2008). The stellar bar is inclined $\sim 4^\circ$ relative to the galactic plane, with the western side above the adopted major axis of the disk. This explains the tilted appearance in the molecular emission (see Figs. 2 and 3).

In addition to these new observations, we use previous interferometric data published by García-Burillo et al. (2001), Fuente et al. (2008) and Weiss et al. (2001b). In Table 1, we give a brief

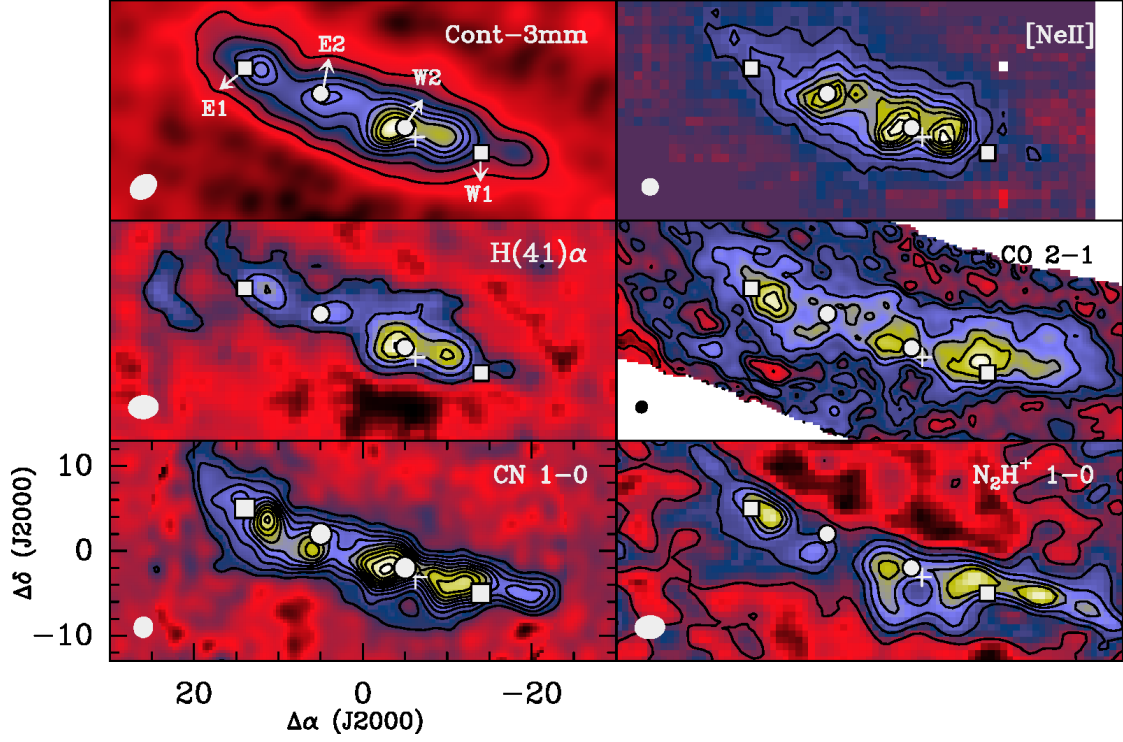


Fig. 2. Map of the continuum emission at 3mm (Fuentes et al. 2008) and line integrated intensity maps of the $12.8 \mu\text{m}$ line of [NeII] (Achtermann & Lacy 1995), $\text{H}(41)\alpha$, $\text{CO } 2 \rightarrow 1$, $\text{CN } 1 \rightarrow 0$ and $\text{N}_2\text{H}^+ 1 \rightarrow 0$ lines. The beam is drawn in the left-down corner of the panels and positions E1, E2, W2 and W1 are indicated by filled polygons. The position of SN 41.9+58 is marked with a white cross. First contour is at 3σ level. Contours levels are: 1.7 mJy/beam, 5 mJy/beam to 35 mJy/beam in steps of 5 mJy/beam (cont-3mm); 0.13 Jy/beam to 1.04 Jy/beam in steps of 0.13 Jy/beam ([NeII]); 4 to 28 in steps of $4 \text{ K} \times \text{km s}^{-1}$ ($\text{H}(41)\alpha$); 200, 400, 600, 800, 1200, 1600, 2000, 2400 $\text{K} \times \text{km s}^{-1}$ (CO); 15.8 to 252.8 in steps of $15.8 \text{ K} \times \text{km s}^{-1}$ (CN); 2.5, 5.0, 7.5, 10.0, 12.5 $\text{K} \times \text{km s}^{-1}$ (N_2H^+). Colour scale is adjusted to the minimum and maximum values in each panel.

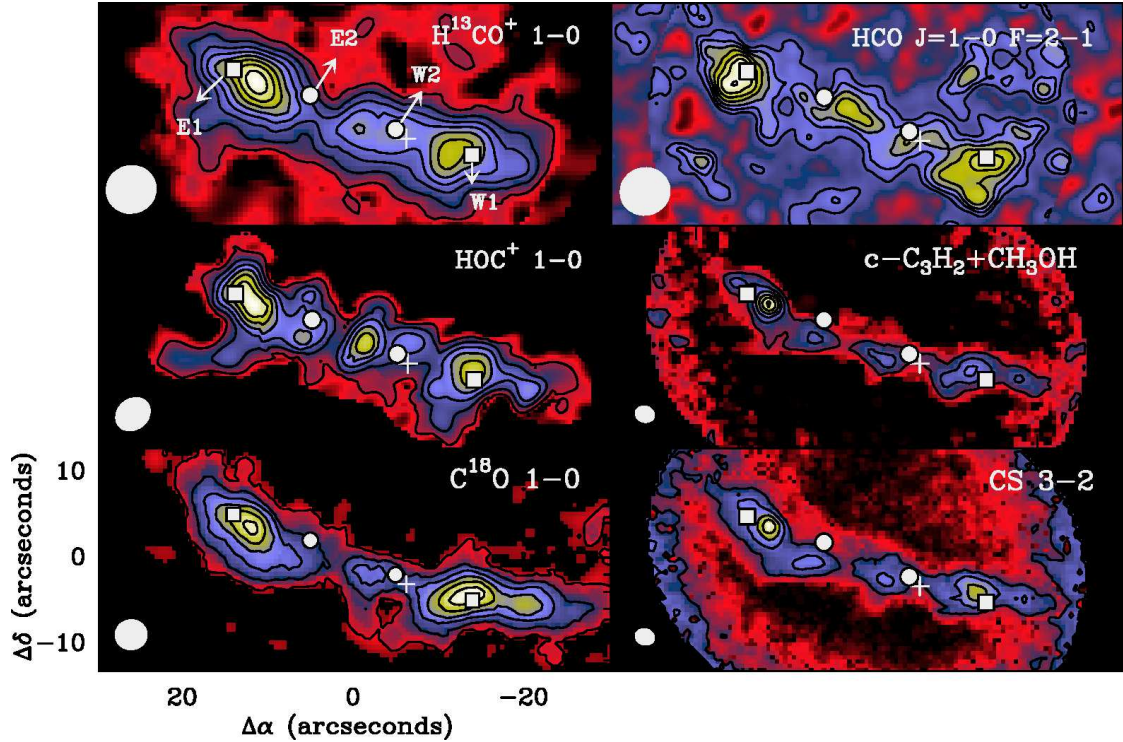


Fig. 3. The same as Fig. 2 for the $\text{H}^{13}\text{CO}^+ 1 \rightarrow 0$, $\text{HCO } 1 \rightarrow 0 \text{ F}=2 \rightarrow 1$, $\text{HOC}^+ 1 \rightarrow 0$, $\text{C}_3\text{H}_2 3_{1,2} \rightarrow 2_{2,1}$, $\text{C}^{18}\text{O } 1 \rightarrow 0$ and $\text{CS } 3 \rightarrow 2$ lines. Contour levels are: 0.6 to 4.6 in steps of $0.6 \text{ K} \times \text{km s}^{-1}$ (H^{13}CO^+); 0.7 to 1.9 in steps of $0.2 \text{ K} \times \text{km s}^{-1}$ (HCO); 0.28, 0.70, 1.12, 1.54, 1.96, 2.38 $\text{K} \times \text{km s}^{-1}$ (HOC^+); 6.4 to 44.8 by steps of $6.4 \text{ K} \times \text{km s}^{-1}$ (C_3H_2); 2, 8, 14, 20, 26, 32 $\text{K} \times \text{km s}^{-1}$ (C^{18}O); 30 to 150 in steps of $30 \text{ K} \times \text{km s}^{-1}$ (CS).

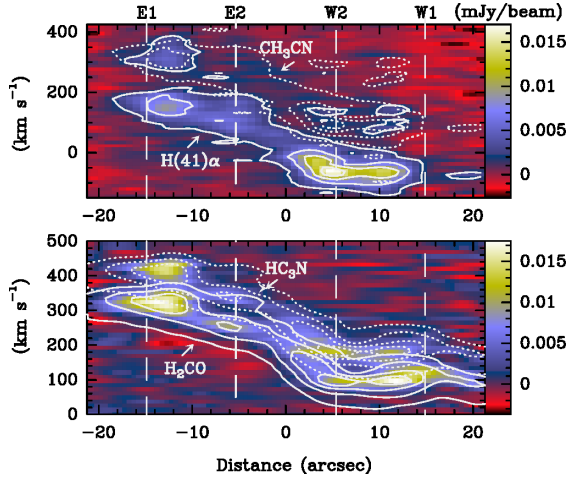


Fig. 4. *Top:* In colour scale, the position-velocity (p-v) diagram along the galactic plane (crossing E1, E2, W2 and W1) of H(41) α . Solid contours are: 2.1 mJy/beam to 16.6 mJy/beam by 4.2 mJy/beam. In dashed lines, the same contours but centered at the frequency of CH₃CN 5₀→4₀ line (91.987 GHz). *Bottom:* In colour scale, the P-V diagram of the H₂CO 2_{0,1}→1_{0,1} line. For comparison, we have drawn in solid contours the levels of the CN 1→0 line: 10.0 mJy/beam to 86.6 mJy/beam by 20.0 mJy/beam. In dashed lines, the same contours at the frequency of the HC₃N 16→15 line. Note that the H₂CO 2_{0,1}→1_{0,1}) and HC₃N 16→15 lines are heavily blended in the inner region.

description of the observations and their more relevant observational parameters.

3. Results

Fig. 1 shows the wide band spectra towards E1. The velocity integrated intensity maps for all the lines detected are shown in Figs. 2 and 3. The maps of the H₂CO 2_{0,2}→1_{0,1} (145.603 MHz) and HC₃N 16→15 (145.601 MHz) are not shown because the lines cannot be deblended in the inner region. In Fig. 4, we show the position-velocity (p-v) diagrams along the galactic plane (straight line across E1, E2, W2 and W1) of the H₂CO 2_{0,2}→1_{0,1}, HC₃N 16→15, CH₃CN 5_k→4_k and H(41) α lines. The CH₃CN 5_k→4_k is only detected towards the outer part of the galaxy and, at 3 σ level, around W2. We subtracted the CH₃CN 5_k→4_k line from the data cube to create the H(41) α map shown in Fig. 2. In Fig. 3, we show the c-C₃H₂ map although we are aware that the line is contaminated with CH₃OH emission. We will discuss this problem in Sect. 4.

3.1. Galactic plane

The emissions of all the species studied in this paper are concentrated in the galactic plane. However, there are some differences in their spatial distributions that we below discuss.

In Fig. 2 we show the integrated intensity maps of the lines that present intense emission towards the inner positions, E2 and W2. E2 and W2 are related with the ring of ionized gas that is associated with the most recent starburst (~ 5 Myr) (Förster-Schreiber et al. 2011). This ring is asymmetric with the western part more intense than the eastern one. The continuum emission at 3mm and the ionized line [NeII] are maxima towards W2 (see Fuente et al. 2008 and Fig. 2). As expected, the emission of H(41) α follows the same spatial distribution. The emissions of

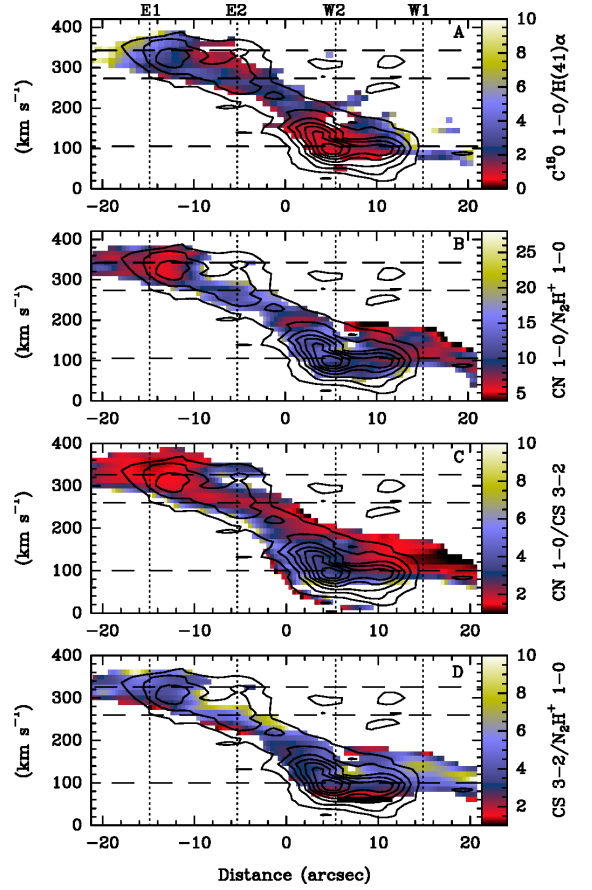


Fig. 5. P-v diagrams along a cut crossing E1, E2, W2 and W1. Contours correspond to the line intensity of H(41) α (2.1 to 16.6 in steps of 2.1 mJy/beam). Colour scale shows the following line intensity ratios (in T_b units): **A**) C¹⁸O 1→0/H(41) α ; **B**) CN 1→0/N₂H⁺ 1→0; **C**) CN 1→0/[CS] 3→2; **D**) CS 3→2/N₂H⁺ 1→0. Horizontal lines correspond to velocities: 100, 270 and 326 km s⁻¹, to make easier the comparison with Fig. 7. Line ratios have been calculated with the original images degraded to common angular resolution of 3.8'' and a velocity resolution of 12 km s⁻¹. The C¹⁸O 1→0/H(41) α line ratio can be considered as an observational measurement of the gas illumination by UV photons. Note that the CN/N₂H⁺ and CN/CS line ratios increase in the highest UV irradiated regions, i.e., minimum values of the C¹⁸O 1→0/H(41) α line ratio.

the molecular lines are, however, more intense in the outer part of the galaxy close to positions E1 and W1, with the only exception of CN that presents its emission peak towards the inner ring following the spatial distribution of the ionized lines. CN is known to present higher abundances in regions with enhanced UV fields (Fuente et al. 1993, 1995; Bachiller et al. 1997; Boger & Sternberg 2005). Its peculiar spatial distribution suggests that the UV radiation from the recently formed stars has a strong impact on the molecular gas chemistry in the inner ring.

The emission of most molecular lines, H¹³CO⁺ 1→0, HOC⁺ 1→0, C¹⁸O 1→0, HCO 1→0, C₃H₂ 3_{1,2}→2_{2,1}, and CS 3→2 is, however, more intense towards the outer positions, E1 and W1 (see Fig. 3). Although all these molecules are brighter in the outer part of the galaxy, the exact positions of their emission peaks differ, especially in the western part. The C₃H₂ 3_{1,2}→2_{2,1}, CS 3→2, H¹³CO⁺ 1→0, and HOC⁺ 1→0 peaks are located 2''–4'' closer to the dynamical center of the galaxy than HCO 1→0.

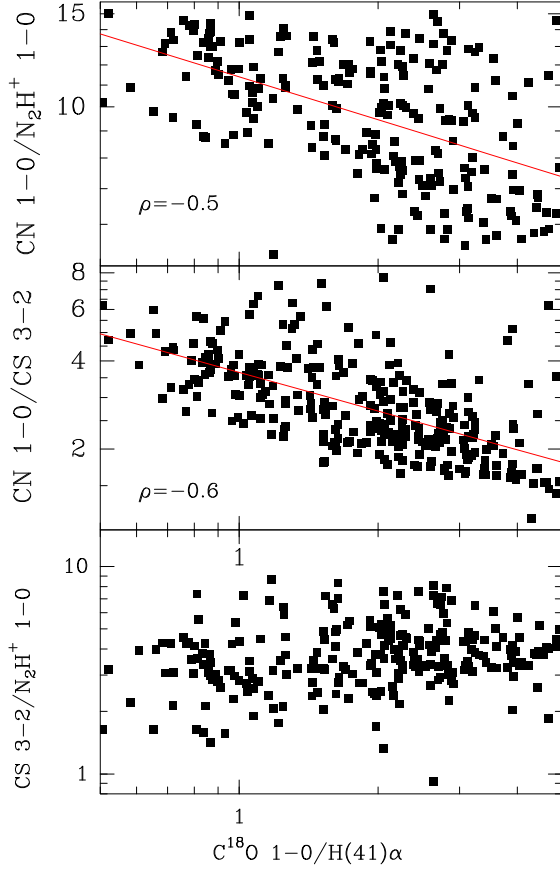


Fig. 6. Correlations between the $\text{C}^{18}\text{O } 1\rightarrow 0/\text{H}(41)\alpha$, $\text{CN } 1\rightarrow 0/\text{N}_2\text{H}^+ 1\rightarrow 0$, and $\text{CS } 3\rightarrow 2/\text{N}_2\text{H}^+ 1\rightarrow 0$ brightness temperature line ratios along the galactic plane shown in Fig. 5. The plots are in logarithmic scale. In order to get a more reliable result avoiding the line borders, we only considered the points within the following range of values: 0.5 and 5 for $\text{C}^{18}\text{O } 1\rightarrow 0/\text{H}(41)\alpha$ line; 5 and 15 for $\text{CN } 1\rightarrow 0/\text{N}_2\text{H}^+ 1\rightarrow 0$; 1 and 6 for $\text{CN } 1\rightarrow 0/\text{CS } 3\rightarrow 2$ between 1 and 6. The results of the least square fitting and the values of the Pearson correlation coefficients are shown in the top and medium panels.

The intense peak of the $\text{c-C}_3\text{H}_2$ line towards E1 is very likely due to the CH_3OH contamination (see Sect. 4).

In Fig. 5 we show the p-v diagrams of the $\text{CN } 1\rightarrow 0/\text{N}_2\text{H}^+ 1\rightarrow 0$, $\text{CN } 1\rightarrow 0/\text{CS } 3\rightarrow 2$ and the $\text{CS } 3\rightarrow 2/\text{N}_2\text{H}^+ 1\rightarrow 0$ line ratios along the plane defined by positions E1, E2, W1 and W2. To perform these diagrams, we have degraded the spatial and spectral resolutions of the three line intensity cubes to common values of $3.8''$ and 12 km s^{-1} , respectively. We adopted $3\times\sigma$ as the threshold for line detection. There is a clear gradient in the $\text{CN } 1\rightarrow 0/\text{N}_2\text{H}^+ 1\rightarrow 0$ line ratio along the galaxy plane, being a factor of ~ 3 higher in the inner region than in E1. For comparison, we show the p-v diagram of the $\text{C}^{18}\text{O } 1\rightarrow 0/\text{H}(41)\alpha$ line ratio that can be considered as an observational tracer of the gas illumination. There are two regions where the $\text{CN } 1\rightarrow 0/\text{N}_2\text{H}^+ 1\rightarrow 0$ takes the peak value of ~ 15 : (i) W2, it is the peak in the $\text{H}(41)\alpha$ line emission and the region with the highest concentration of HII regions; and (ii) E2, the emission of the $\text{H}(41)\alpha$ line is lower than in W2 but the molecular gas column density is also lower, especially in the $\sim 326 \text{ km s}^{-1}$ component that is not detected in N_2H^+ (see Sect. 3.2); as a consequence, the molecular gas is very likely immersed in a high UV field (see Fig. 5, A). The $\text{CN } 1\rightarrow 0/\text{CS } 3\rightarrow 2$ line ratio has a ratio $\sim 1-2$ along the cut and increases to

~ 5 only in the two enhanced UV field regions described above (see Fig. 5, C). The variations of these two molecular line ratios are not hazardous but seems related with the distribution of the ionized gas suggesting that UV photons are the driving agent of the molecular chemistry. In Fig. 6 we show the log-log correlation diagrams between the $\text{CN } 1\rightarrow 0/\text{N}_2\text{H}^+ 1\rightarrow 0$ and $\text{CN } 1\rightarrow 0/\text{CS } 3\rightarrow 2$ line ratios, and $\text{C}^{18}\text{O } 1\rightarrow 0/\text{H}(41)\alpha$. As expected there is a good (anti-)correlation between these ratios at low extinctions (low values of $\text{C}^{18}\text{O } 1\rightarrow 0/\text{H}(41)\alpha$). At high extinctions, the dispersion is larger since we can have PDRs (diffuse clouds, the external layers of giant molecular clouds, dense gas around Herbig Ae/Be stars) that do not emit in $\text{H}(41)\alpha$ but also present enhanced CN abundances (see e.g. Fuente et al. 1993, 1995, Liszt et al. 2001). On the contrary, although with a large dispersion, the $\text{CS } 3\rightarrow 2/\text{N}_2\text{H}^+ 1\rightarrow 0$ line ratio is ~ 5 towards all positions.

3.2. Vertical distribution of the molecular emission

M 82 is associated with a kpc-scale outflow with the gas coming towards us in the northern part. Optical and near infrared lines look asymmetric with the most intense half towards the north where the radio continuum chimneys are located (Wills et al. 1999). This asymmetry is also detected in the emission of $\text{H}(41)\alpha$ which proves that it is not a consequence of the dust extinction but to the spatial distribution of the massive star forming regions located in the northern half of the disk (see Fig. 7). On the contrary, the molecular emission extends to $\sim 7.5''$ south from the galactic plane following the molecular supershell around the supernova remnant SN 41.9+58. Regarding the molecular emission, there are important differences between the vertical spatial distribution of the different species.

One interesting case is the comparison of the HCO^+ and HOC^+ emissions. Fuente et al. (2008) found a clear north-south gradient in the $[\text{HCO}^+]/[\text{HOC}^+]$ ratio being this ratio maximum towards the southern part of the supershell associated to SN 41.9+58. The maximum in the HOC^+ emission is shifted $\sim 2.5''$ north relative to H^{13}CO^+ , i.e. closer to the ionized layer traced by $\text{H}(41)\alpha$. Fuente et al. (2008) interpreted this gradient as a change in the global ionization degree of the molecular clouds.

We used the CN, N_2H^+ , CS and $\text{H}(41)\alpha$ images to make a detailed study of the kinematics and spatial distribution of the molecular gas in the direction perpendicular to the galaxy plane. In Fig. 7 we show the p-v diagrams in the vertical direction across E2, the dynamic center of the galaxy, and W2. In these diagrams, the velocity axis has been re-binned to channels of 12 km s^{-1} .

Towards E2, several velocity components are detected in the $\text{H}(41)\alpha$ and molecular lines. All these components are within the range of velocities of the x2 bar orbits, $\pm 120 \text{ km s}^{-1}$ (Greve 2011). The component at $\sim 260 \text{ km s}^{-1}$ is the most intense in molecular emission and is detected in CN, N_2H^+ and CS. However, the component at $\sim 326 \text{ km s}^{-1}$ is well detected in the CN $1\rightarrow 0$ line, only tentatively detected in CS $3\rightarrow 2$ ($3\times\sigma$ level) and remains undetected in the $\text{N}_2\text{H}^+ 1\rightarrow 0$ line. This component is associated with a secondary peak in the $\text{H}(41)\alpha$ emission. In the right panel, we show the $\text{CN } 1\rightarrow 0/\text{N}_2\text{H}^+ 1\rightarrow 0$ line intensity ratio. It varies between ~ 10 and ~ 15 along this cut with the peaks following the peaks of the $\text{H}(41)\alpha$ emission.

Several velocity molecular components are also detected towards W2. In this case, we can also observe a layered structure in the vertical direction with the $\text{H}(41)\alpha$ and CN emission being extended towards north while N_2H^+ emission is more extended towards the south. Again, there are important chemical differ-

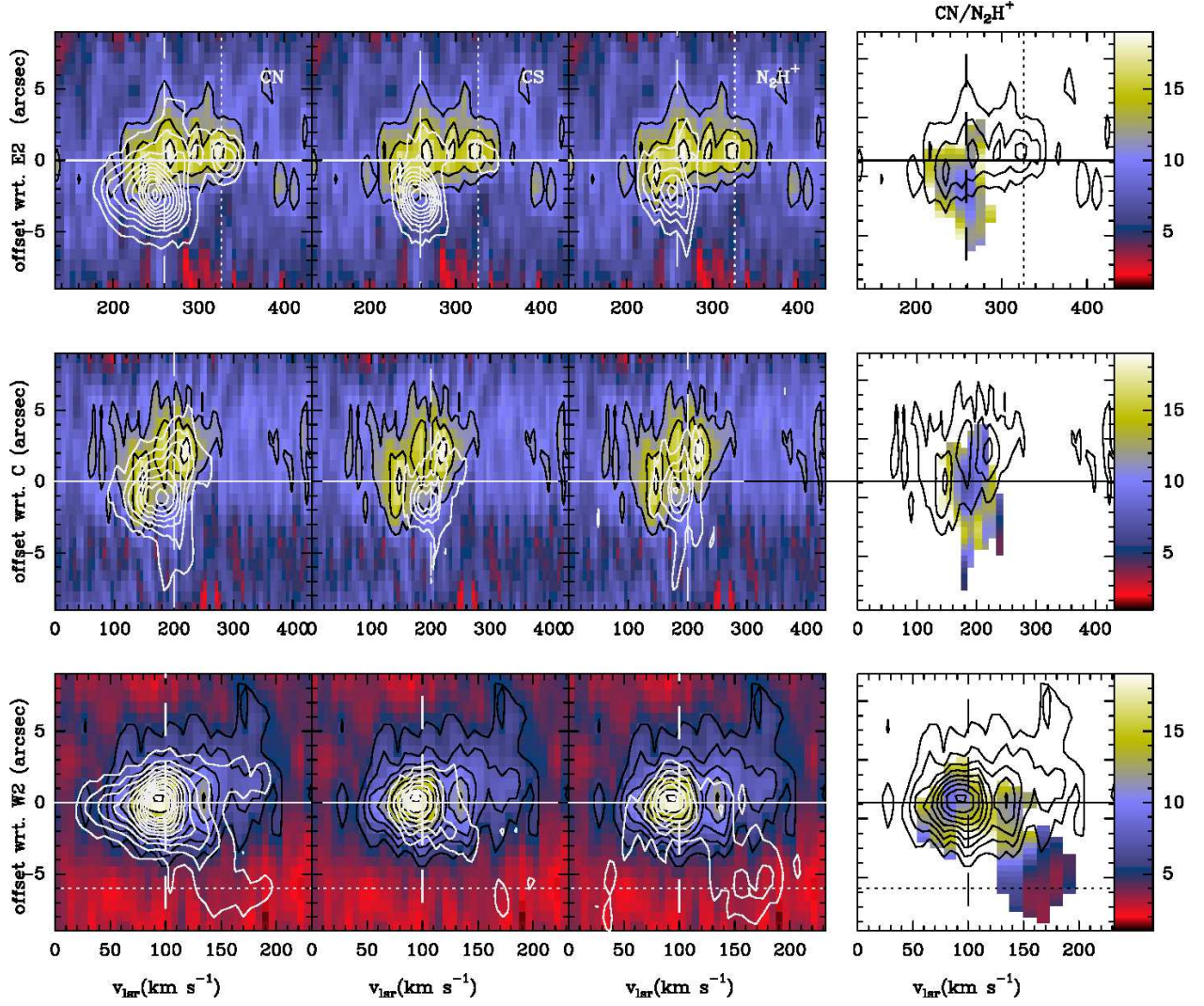


Fig. 7. P-v diagrams along cuts perpendicular to the galactic plane at E2 (top), the (0,0) position (middle) and W2 (bottom). Colour scale and black contours correspond to the H(41) α emission. White contours are intensities of the CN 1 \rightarrow 0, CS 3 \rightarrow 2 and N₂H⁺ 1 \rightarrow 0 lines. First contours ($3\times\sigma$) and steps are: 10 mJy/beam for CN and CS; 2 mJy/beam for N₂H⁺ and H(41) α . The CN 1 \rightarrow 0/N₂H⁺ 1 \rightarrow 0 line intensity (in T_b units) ratio along these cuts is shown in the right column. The images have been degraded to an angular resolution of $3.8''$ and a velocity resolution of 12 km s^{-1} to perform this line ratio. Vertical lines indicate of the position of the velocity components discussed in the text.

ences between the $\sim 100 \text{ km s}^{-1}$ (north) and $\sim 160 \text{ km s}^{-1}$ (south) components. The north component is more intense in CN and CS, while the south component is brighter in the N₂H⁺ emission. The CN 1 \rightarrow 0/N₂H⁺ 1 \rightarrow 0 line intensity ratio shows an excellent correlation with the H(41) α emission, with a contrast of a factor of ~ 5 between the north and south components. The lowest values, $\sim 2-3$, are found towards the south, and are even lower than those observed in the outer part (E1, W1) of the galaxy (see Fig. 5).

For comparison, we also show the p-v diagram across the dynamic center of the galaxy. The H(41) α emission is detected shifted towards the north compared with the molecular emission. Similarly to the vertical cut across E2, the CN 1 \rightarrow 0/N₂H⁺ 1 \rightarrow 0 line intensity ratio vary between ~ 10 and ~ 15 with the peaks towards the peaks of the H(41) α emission, suggesting that it is a general trend all over the galactic nucleus.

4. Column densities towards selected positions

4.1. CN, N₂H⁺, c-C₃H₂ and CS

The high angular and spectral resolutions provided by our new data: CN 1 \rightarrow 0, N₂H⁺ 1 \rightarrow 0, H(41) α , CS 3 \rightarrow 2 and C₃H₂ 3 \rightarrow 2, allow us to carry out a detailed chemical study of the interstellar medium in M 82. The spectral cubes of all these lines have been degraded to a common angular resolution of $3.8''$ ($\approx 70 \text{ pc}$) and a channel width of 12.8 km s^{-1} , that are typical values for the size and linewidth of a giant molecular cloud (see e.g. Murray 2011). From these data, we have selected 12 molecular position-velocity peaks (see Fig. 8) to carry out our chemical modeling. The selection criteria are: the knots must be (i) intense and (ii) well identified in velocity and position. In addition, the whole set must represent the variety of physical and chemical conditions in the galaxy. The intense and compact emission towards these positions minimizes the uncertainties due to spatial filtering effects. The selected knots are listed Table 2 and indicated in Fig. 8 and Figs. A.1 to A.3.

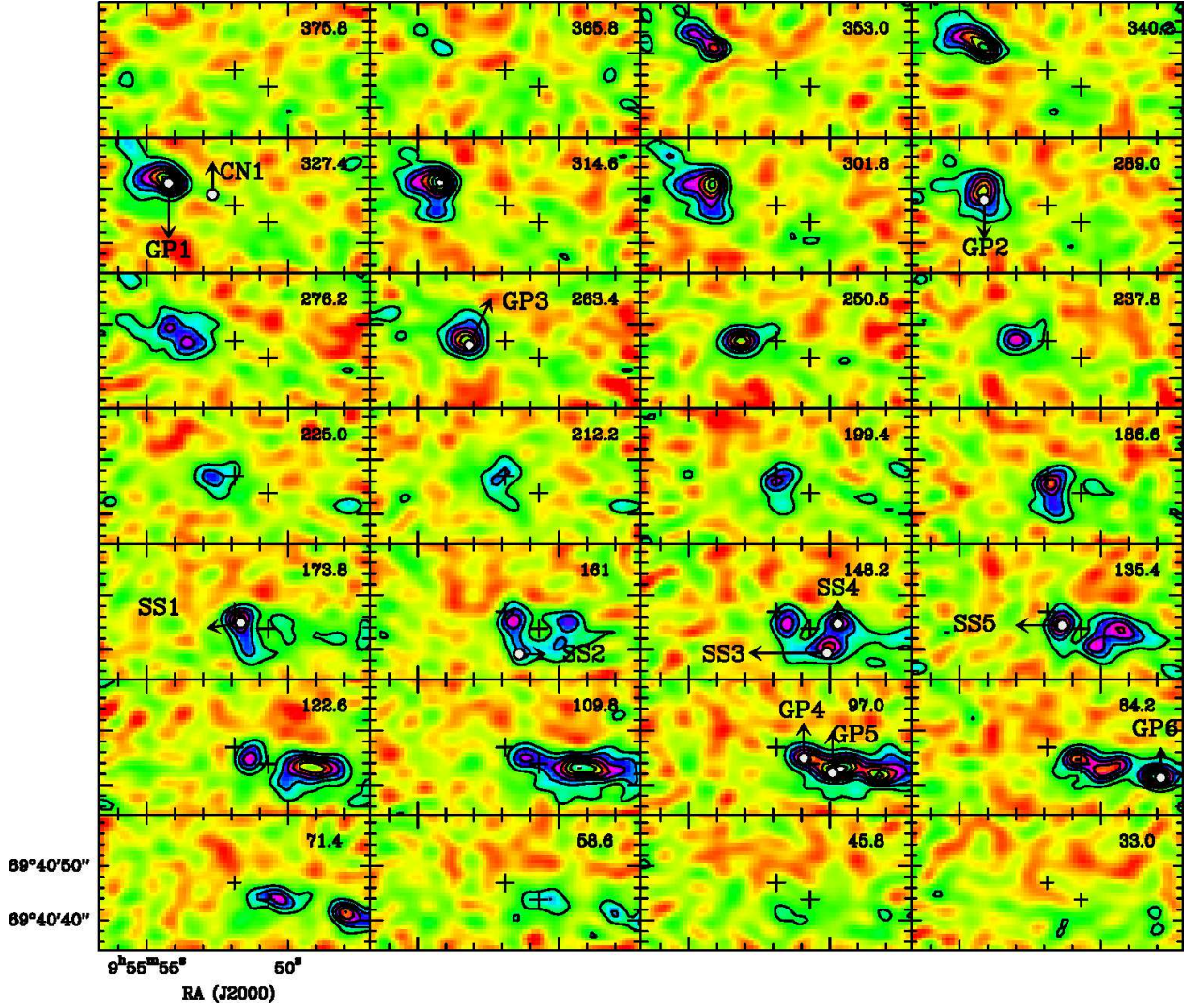


Fig. 8. Spectral maps of the N_2H^+ $1\rightarrow 0$ line convolved to an angular resolution of $3.8''$. To increase the S/N ratio, the velocity resolution has been degraded to 12.8 km s^{-1} . The number in the right-upper corner indicates the central channel velocity. First contour and step are 0.028 K ($\sim 3\times\sigma$). Crosses indicate the dynamical center of the galaxy and the position of SN 41.9+58.

GP1 to GP6 are compact molecular peaks along the galactic plane that follow the velocity pattern of the x_1 and x_2 bar orbits. These knots have been detected in all molecular lines (see Fig. 8 and Figs. A.1-A.3). We have added 5 positions, SS1 to SS5, placed in the supershell associated to SN 41.9+58. Note that SS1 and SS2 are very close to GP4 in the plane of sky and are only distinguishable because of their different velocities. Examining the CN spectral maps, we identified one well defined CN emission peak with weak counterpart in the other species. We will refer to this position as CN1 and corresponds to the $\sim 326 \text{ km s}^{-1}$ component towards E2 (see Figs. 7 and A.1). Fig. A.3 shows the $\text{H}(41)\alpha$ PdBI spectral maps. This line probes the spatial distribution of the ionized gas that is closely related to the local UV field. GP4 is the most intense position in this radio recombination line. Secondary peaks are spatially coincident with GP1, CN1 and GP5 showing the presence of ionized gas at these positions. The absence of $\text{H}(41)\alpha$ emission towards SS2 and SS3 proves the existence of a lower UV field in the southern part of the supershell. Therefore, our selected positions are representative of the different physical conditions, in particular the mean UV field, within this galaxy.

We have estimated the CN, N_2H^+ , CS and C_3H_2 molecular column densities using the LVG code MADEx (Cernicharo 2012). Our observations do not allow a multitransitional study. Instead, we need to assume a uniform layer with constant physical conditions. On basis of CO and its isotopologues, Weiss et al. (2001b) derived densities of $n(\text{H}_2) \sim 5 \times 10^4 \text{ cm}^{-3}$ and gas kinetic temperatures ranging from $\sim 50 \text{ K}$ towards the E1 and W1 positions to $\sim 150 \text{ K}$ towards E2 and W2. Later, Fuente et al. (2005) determined densities of $1 \times 10^5 \text{ cm}^{-3}$ from single-dish data of the CN $1\rightarrow 0$ and $2\rightarrow 1$ lines. Higher densities, $\sim 5 \times 10^5 \text{ cm}^{-3}$, were estimated by Fuente et al. (2008) using the high excitation $J=3\rightarrow 2$ and $4\rightarrow 3$ lines of HCO^+ . Bayet et al. (2009) proposed two components to fit the CS lines with densities of $\sim 10^5 \text{ cm}^{-3}$ and $6 \times 10^5 \text{ cm}^{-3}$ for the diffuse and dense components, respectively. These estimates proved that, as expected, different density components coexist within our beam. Since we are dealing with molecules with large dipole moments, we considered that the emission is dominated by dense gas with $n(\text{H}_2) > 1 \times 10^5 \text{ cm}^{-3}$. To estimate the molecular column densities and the uncertainties in our calculations we run a grid of LVG models with $n(\text{H}_2)$ varying from 1×10^5 – $5 \times 10^5 \text{ cm}^{-3}$ and $T_k = 50, 150 \text{ K}$ and adopted the average value. The hyperfine structures of CN and N_2H^+

have not been considered in our calculations because of the large linewidths. The estimated column densities are shown in Table 2. The errors correspond to the minimum and maximum values obtained in our grid, i.e., these errors do not account for the observational errors, which are lower, but for the uncertainty in the physical conditions. In general, the uncertainties in the obtained column densities are within a factor of 2.

In our calculations we assumed that all the emission at 145.089 GHz comes from the $c\text{-C}_3\text{H}_2$ carrier that is not true for some positions. Methanol was firstly detected by Martín et al. (2006) in M 82. Based on the kinematical and spatial distribution, they concluded that the emission is mainly coming from the intense east and west knots at the outer part of the galaxy. Later, Aladro et al. (2011) performed a single-dish multitransitional study of CH_3OH and $c\text{-C}_3\text{H}_2$ towards a position close to E1 and derived their column densities and rotational temperatures. We assumed these values to predict the expected CH_3OH and $c\text{-C}_3\text{H}_2$ line intensities and obtained that $\sim 50\%$ of the emission must belong to each carrier towards E1. According to these results the $c\text{-C}_3\text{H}_2$ column density is overestimated by a factor of ~ 2 in E1. Taking into account the similarities between the molecular chemistry in E1 and W1, we consider that, very likely, we have a similar contamination, i.e. $\sim 50\%$, towards W1.

In Table 2, we also show the $[\text{CN}]/[\text{N}_2\text{H}^+]$, $[\text{CS}]/[\text{N}_2\text{H}^+]$ and $[\text{CN}]/[\text{CS}]$ column density ratios towards the selected molecular knots. These values have been estimated using the same procedure as for the column densities. We run a grid of LVG models and adopted the average value of the fitted column density ratios. When molecules with similar excitation conditions are selected, this method minimizes the uncertainty due to the assumed physical conditions, being the uncertainties in the column density ratios lower than those of the individual column densities (see Table 2).

Significant variations, i.e. higher than the uncertainties, are found in the $[\text{CN}]/[\text{N}_2\text{H}^+]$ ratio across the galaxy. This ratio takes values ≈ 30 in GP1 and GP6 located in the outer $x1$ orbits and increases to ≈ 80 towards GP4. Values > 50 are found towards GP5 and SS1, both close to W2. The minimum value, $[\text{CN}]/[\text{N}_2\text{H}^+] \approx 19$, is found in the southern part of the supershell. In Fig. 9 we compare the obtained column density ratios with the integrated intensity maps of the $\text{N}_2\text{H}^+ 1\rightarrow 0$, $\text{H}(41)\alpha$ lines and $\text{SiO } 2\rightarrow 1$ lines. It is remarkable that there is a good correlation between the values of the $[\text{CN}]/[\text{N}_2\text{H}^+]$ ratio and the emission of the $\text{H}(41)\alpha$ line, supporting the interpretation that the variations of the $[\text{CN}]/[\text{N}_2\text{H}^+]$ ratio are related to the variations of the local UV field. We do not find any correlation between the $[\text{CN}]/[\text{N}_2\text{H}^+]$ ratio and the SiO emission.

The $[\text{CN}]/[\text{CS}]$ ratio behaves similarly to $[\text{CN}]/[\text{N}_2\text{H}^+]$. It takes values ≈ 3.5 in GP1 and GP6 located in the outer $x1$ orbits and increases to > 5 towards GP4, GP5, and SS1. In the case of CN1, we estimate a higher value of, $[\text{CN}]/[\text{CS}] \approx 10$. There is a good correlation between the $[\text{CN}]/[\text{CS}]$ ratio and the $\text{H}(41)\alpha$ emission.

Contrary to the $[\text{CN}]/[\text{N}_2\text{H}^+]$ and $[\text{CN}]/[\text{CS}]$ ratios, the $[\text{CS}]/[\text{N}_2\text{H}^+]$ ratio remains quite constant across the galactic plane with values around ~ 12 . There is no evidence of variation of this ratio with the local UV field. When comparing the galactic plane positions with those of the supershell, we realized that the ratio tends to be a factor of 2 lower in the southern part of the supershell, although always within the uncertainty of our calculations.

We used the C^{18}O map from Weiss et al. (2001b) to determine the total molecular hydrogen column densities and absolute fractional abundances. The C^{18}O column densities vary by

only a factor of ~ 2 among the different knots with the largest values in GP1 and GP6. Molecular abundances have been derived from the $\text{N}(\text{X})/\text{N}(\text{C}^{18}\text{O})$ column density ratio assuming $[\text{C}^{18}\text{O}]/[\text{C}^{12}\text{O}] = 0.005$ and $[\text{C}^{12}\text{O}] = 4 \times 10^{-5}$, which are the average values derived by Weiss et al. (2001b) on basis of their multitransitional study of CO , ^{13}CO and C^{18}O . Note that these values correspond to a $^{16}\text{O}/^{18}\text{O}$ ratio of 200 which is different from the Milky Way standard value of $\sim 500\text{--}600$. We are assuming a constant C^{18}O abundance all over the galaxy which is an approximation since the C^{18}O abundance is dependent on the environment (UV flux, density, temperature). However, we are interested in the dense molecular gas ($n(\text{H}_2) > 1 \times 10^5 \text{ cm}^{-3}$) and the C^{18}O abundance is expected to remain roughly constant in this component. Following this procedure we derived the molecular abundances shown in Table 2. The N_2H^+ abundance is $\sim 3 \times 10^{-11}$ for all the positions, corroborating that N_2H^+ is a good tracer of the dense molecular gas. An abundance of a few 10^{-10} is measured for CS. Small changes, less of a factor of 2, are found in the abundances of this species that are within the uncertainties of our calculations. Only the CN abundance presents significant variations within the galaxy, being larger by a factor ~ 3 in GP4 than in the outer positions, GP1 and GP6, and the southern supershell positions, SS2 and SS3.

4.2. Other species: H_2CO , HC_3N and CH_3CN

In order to have a more comprehensive view of the chemistry in M 82 we have compared our new data with previous interferometric images. For this aim, we degraded the angular resolution of all our images to $\approx 5.9''$ (≈ 111 pc), which is the lowest from the data set shown in Table 1, and used the total velocity integrated line intensity in our calculations. The Gaussian fit parameters towards E1, E2, W2 and W1 are shown in Table A.1.

Column densities and column density ratios were calculated following the same procedure as in Sect. 4.1. In Table 3, we show the values obtained for E1, E2, W2 and W1. The $[\text{CS}]/[\text{H}^{13}\text{CO}^+]$ and $[\text{H}^{13}\text{CO}^+]/[\text{C}^{18}\text{O}]$ are quite uniform across the galaxy. This suggests that CS, H^{13}CO^+ and C^{18}O are good tracers of dense gas in a wide range of physical conditions. According to these results, E1 and W1 present the highest total molecular hydrogen column densities. This is consistent with the detection of complex molecules like NH_3 , HC_3N , CH_3CN and CH_3OH towards them (Weiss et al. 2001a, Martín et al. 2006, Aladro et al. 2011). The small hydrocarbons $c\text{-C}_3\text{H}_2$ and C_4H are also good tracers of low and high UV PDRs (Fuente et al. 2003, Pety et al. 2005, Pilleri et al. 2013, Cuadrado et al. 2014). Taking into account that the abundance of $c\text{-C}_3\text{H}_2$ is very likely overestimated by a factor of ~ 2 in E1 and W1 (see Sect. 4), we conclude that the abundance of $c\text{-C}_3\text{H}_2$ could be enhanced by a factor of ~ 3 in the inner $x2$ orbits, in agreement with the trend observed in CN. Moreover, the derived H_2CO abundance is similar to that derived by Guzmán et al. (2013, 2014) in the Horsehead nebula and consistent with the interpretation of the H_2CO emission coming from PDRs. Summarizing, the overall chemical behavior observed in M 82 is well interpreted as the consequence of the effect of UV radiation on the molecular chemistry. This produces an increase in the abundance of PDR tracers (CN, $c\text{-C}_3\text{H}_2$, H_2CO) towards E2 and W2, following the spatial distribution of HII regions. The detection of complex molecules shows that a fraction of the gas is protected from the UV radiation in the interior of large molecular clouds. The amount of gas in this shielded component is higher in the outer $x1$ bar orbits.

We remind that the position W2 is related with the supernova explosion SN 41.9+58 that is launching ionized gas out

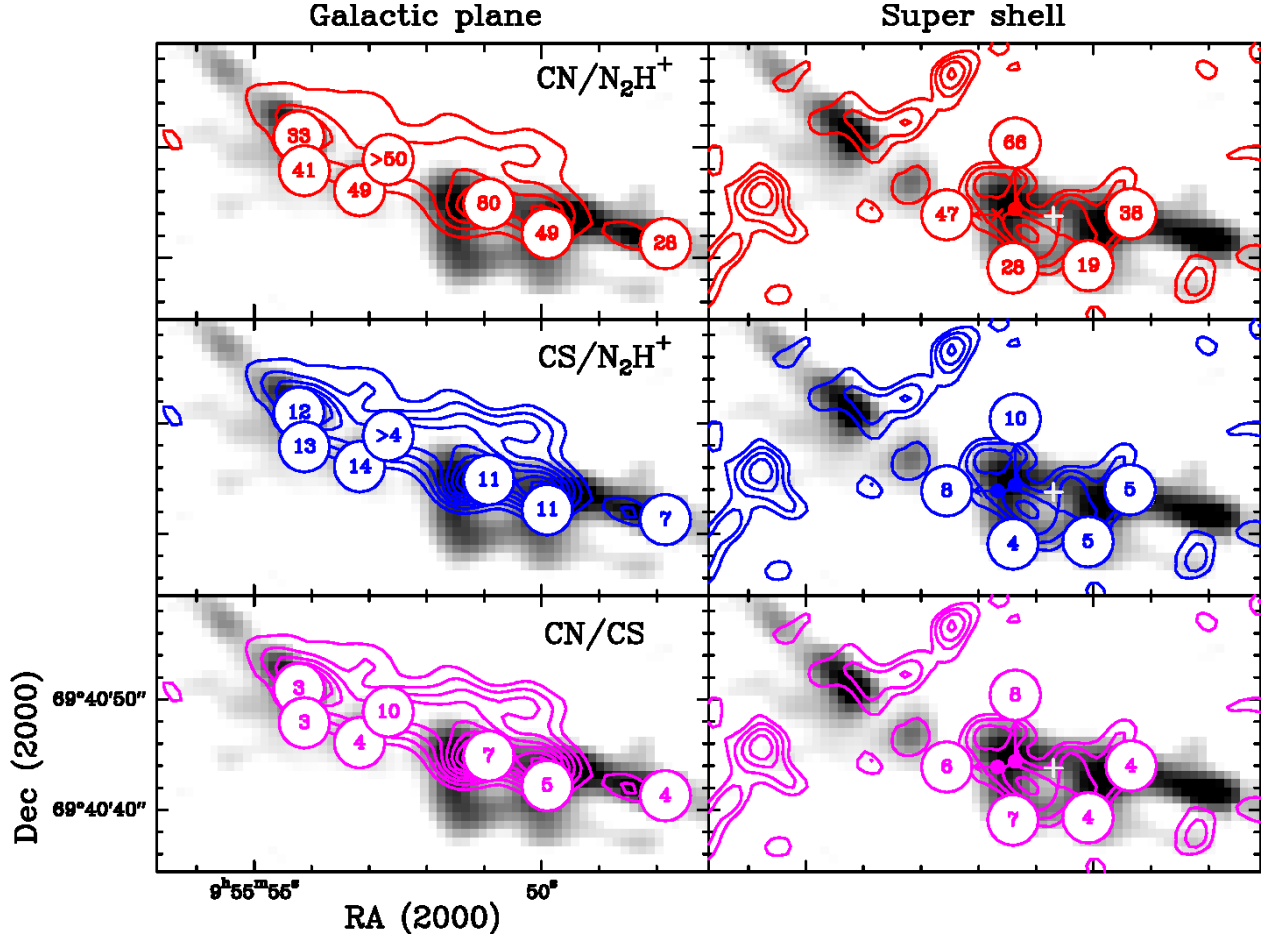


Fig. 9. $[\text{CN}]/[\text{N}_2\text{H}^+]$, $[\text{CS}]/[\text{N}_2\text{H}^+]$ and $[\text{CN}]/[\text{CS}]$ abundance ratios for the positions listed in Table 2 in the galactic plane (left) and the supershell associated with SN 41.9+58 (right) superposed to the N_2H^+ $1 \rightarrow 0$ integrated intensity map (grey scale). For comparison, on the left column we plot the contours of the integrated intensity emission of the H (41) α line, and on the right, the integrated intensity emission of the SiO $2 \rightarrow 1$ line (García-Burillo et al. 2001). The white cross indicates the position of SN 41.9+58.

Table 2. Selected regions for the chemical model¹.

Point	Offset ($''$)		Vel (km s^{-1})	N(C 18 O) ($\times 10^{16} \text{ cm}^{-2}$)	X(CN) ($\times 10^{-9}$)	X(N $_2$ H $^+$) ($\times 10^{-11}$)	X(o-C $_3$ H $_2$) 2 ($\times 10^{-10}$)	X(CS) ($\times 10^{-10}$)	[CN]/[N $_2$ H $^+$]	[CS]/[N $_2$ H $^+$]	[CN]/[CS]
GP1	+12.1	+4.1	327.4	2.2 $^{+1.2}_{-1.0}$	0.9 $^{+0.8}_{-0.3}$	3.0 $^{+1.8}_{-1.3}$	3.2 $^{+3.0}_{-1.7}$	3.0 $^{+3.9}_{-1.1}$	33 $^{+17}_{-11}$	12 $^{+8}_{-6}$	3.0 $^{+0.5}_{-0.3}$
GP2	+11.6	+1.0	289.0	1.8 $^{+1.0}_{-0.8}$	1.0 $^{+0.3}_{-0.3}$	2.8 $^{+1.3}_{-1.4}$	2.6 $^{+2.7}_{-1.4}$	3.2 $^{+3.6}_{-1.2}$	41 $^{+22}_{-13}$	13 $^{+10}_{-6}$	3.3 $^{+0.3}_{-0.5}$
GP3	+6.6	-0.8	263.4	1.8 $^{+1.0}_{-0.8}$	1.4 $^{+1.0}_{-0.5}$	3.0 $^{+1.4}_{-1.6}$	3.0 $^{+3.3}_{-1.5}$	3.8 $^{+4.3}_{-1.5}$	49 $^{+23}_{-16}$	14 $^{+10}_{-6}$	3.7 $^{+0.6}_{-0.7}$
GP4	-5.1	-2.0	97.0	0.9 $^{+0.5}_{-0.4}$	3.0 $^{+2.1}_{-1.1}$	4.3 $^{+2.0}_{-2.1}$	2.6 $^{+2.8}_{-1.4}$	3.5 $^{+5.2}_{-1.2}$	80 $^{+34}_{-28}$	11 $^{+8}_{-5}$	7.4 $^{+1.4}_{-1.5}$
GP5	-10.4	-4.7	97.0	1.9 $^{+1.1}_{-0.9}$	1.4 $^{+1.0}_{-0.4}$	3.2 $^{+1.5}_{-1.5}$	2.4 $^{+2.7}_{-1.7}$	2.6 $^{+3.6}_{-1.9}$	49 $^{+23}_{-16}$	11 $^{+7}_{-5}$	4.8 $^{+0.9}_{-0.6}$
GP6	-21.1	-5.6	84.2	2.1 $^{+1.1}_{-1.0}$	0.8 $^{+0.4}_{-0.3}$	3.1 $^{+1.5}_{-1.5}$	1.5 $^{+1.7}_{-0.8}$	1.8 $^{+1.9}_{-0.7}$	28 $^{+15}_{-10}$	7 $^{+5}_{-3}$	3.8 $^{+0.9}_{-0.6}$
SS1	-1.2	-2.0	173.8	1.0 $^{+0.5}_{-0.3}$	2.0 $^{+1.6}_{-0.7}$	4.8 $^{+2.3}_{-1.9}$	3.1 $^{+3.5}_{-1.2}$	2.9 $^{+4.3}_{-1.0}$	47 $^{+23}_{-16}$	8 $^{+5}_{-3}$	6.2 $^{+1.0}_{-1.2}$
SS2	-2.6	-7.8	161.0	0.6 $^{+0.3}_{-0.3}$	0.9 $^{+0.8}_{-0.3}$	3.8 $^{+1.9}_{-1.8}$	1.4 $^{+1.6}_{-0.7}$	1.1 $^{+1.3}_{-0.7}$	28 $^{+15}_{-10}$	4 $^{+3}_{-2}$	7.5 $^{+1.4}_{-1.4}$
SS3	-9.4	-7.6	148.2	1.4 $^{+0.7}_{-0.7}$	0.5 $^{+0.4}_{-0.2}$	2.7 $^{+1.4}_{-1.3}$	1.4 $^{+1.7}_{-0.7}$	1.0 $^{+1.5}_{-0.4}$	19 $^{+11}_{-7}$	5 $^{+4}_{-3}$	4.2 $^{+0.6}_{-0.8}$
SS4	-13.3	-2.9	148.2	1.5 $^{+0.7}_{-0.7}$	0.9 $^{+0.7}_{-0.3}$	2.7 $^{+1.3}_{-1.3}$	2.2 $^{+2.1}_{-1.0}$	2.4 $^{+2.6}_{-1.1}$	38 $^{+19}_{-13}$	5 $^{+4}_{-3}$	4.0 $^{+0.7}_{-0.7}$
SS5	-2.8	-2.5	135.4	1.1 $^{+0.5}_{-0.5}$	2.4 $^{+1.9}_{-0.8}$	4.2 $^{+2.0}_{-2.0}$	2.6 $^{+2.9}_{-1.3}$	2.6 $^{+3.9}_{-0.9}$	66 $^{+29}_{-23}$	10 $^{+7}_{-5}$	8.3 $^{+1.6}_{-1.7}$
CN1	+4.0	+2.0	327.4	0.3 $^{+0.1}_{-0.1}$	2.0 $^{+1.8}_{-0.7}$	<4.0*	<3.0*	1.8 $^{+3.1}_{-0.6}$	>50	>4	9.8 $^{+2.0}_{-2.0}$

¹Relative abundances wrt. H₂; ² Contaminated with methanol (see text); * 3 σ limit.

of the galaxy plane. The detection of SiO by García-Burillo et al. (2001) proved the existence of shocks and their effect on the gas chemistry. H₂CO, CH₃OH and CS are considered good tracers of shocks in galactic and extra-galactic environments (see e.g. Bachiller et al. 2001, García-Burillo et al. 2000, Usero et

al. 2006). However, our data do not present any evidence of CS abundance enhancement because of possible shocks. In fact, the $[\text{CS}]/[\text{N}_2\text{H}^+]$ ratio is slightly lower in the super-shell. This suggests that only a small fraction of the gas is affected by shocks, which is also consistent with the low average SiO abundance

Table 3. Fractional abundances and abundance ratios.

	E1	E2	W2	W1
$N(C^{18}O) (\times 10^{16})$	10^{+6}_{-4}	$4.1^{+2.5}_{-1.7}$	$4.8^{+2.7}_{-2.0}$	11^{+7}_{-4}
$X(CN) (\times 10^{-9})$	$1.4^{+0.5}_{-0.4}$	$3.2^{+1.0}_{-0.8}$	$4.0^{+1.4}_{-1.0}$	$1.2^{+3.8}_{-0.3}$
$X(N_2H^+) (\times 10^{-11})$	$2.4^{+0.6}_{-0.6}$	$3.1^{+0.6}_{-0.4}$	$4.4^{+0.8}_{-0.9}$	$2.0^{+0.4}_{-0.4}$
$X(CS) (\times 10^{-10})$	$5.2^{+2.4}_{-1.8}$	$7.2^{+3.6}_{-2.5}$	$7.8^{+3.6}_{-2.8}$	$4.3^{+2.0}_{-1.4}$
$X(H^{13}CO^+) (\times 10^{-11})$	$1.8^{+0.7}_{-0.7}$	$1.3^{+0.6}_{-0.6}$	$2.4^{+1.0}_{-0.8}$	$1.3^{+0.5}_{-0.3}$
$X(o-C_3H_2) (\times 10^{-10})$	$2.0^{+1.2}_{-0.7}$	$2.8^{+1.8}_{-1.8}$	$3.4^{+2.2}_{-2.2}$	$2.4^{+2.3}_{-1.6}$
$X(p-H_2CO) (\times 10^{-11})$	$7.4^{+5.8}_{-3.6}$	$>9.6^{+7.8}_{-4.8}$	$>5.6^{+4.4}_{-2.8}$	$4.6^{+3.8}_{-2.2}$
$X(HC_3N) (\times 10^{-11})$	$8.1^{+12}_{-6.5}$	$<13^{+19}_{-11}$	$<31^{+46}_{-25}$	$5.3^{+8.8}_{-4.2}$
$X(CH_3CN) (\times 10^{-11})$	$1.4^{+2.0}_{-0.6}$	$<1.0^{**}$	$<0.8^{**}$	$1.0^{+1.3}_{-0.4}$
$[CN]/[N_2H^+]$	56^{+13}_{-7}	101^{+29}_{-16}	92^{+18}_{-14}	58^{+14}_{-8}
$[CN]/[CS]$	$2.8^{+1.8}_{-1.0}$	$4.7^{+1.5}_{-1.7}$	$5.6^{+1.6}_{-2.1}$	$2.9^{+0.9}_{-0.9}$
$[CS]/[N_2H^+]$	20^{+6}_{-6}	17^{+13}_{-8}	23^{+9}_{-8}	21^{+7}_{-7}
$[H^{13}CO^+]/[N_2H^+]$	$0.7^{+0.2}_{-0.2}$	$0.5^{+0.2}_{-0.2}$	$0.5^{+0.2}_{-0.2}$	$0.6^{+0.1}_{-0.1}$

Notes. Beam ($5.9''$) average column densities resulting from LVG calculations in a grid with $T_k=50$ – 150 K, and $n(H_2)=1\times 10^5$, 5×10^5 . Errors correspond to the minimum and maximum values in the grid. * Reasonable guess since the HC_3N and H_2CO are blended at this position. ** Upper limit have been derived assuming $\Delta v=50$ km s $^{-1}$, $T_k=50$ K and $n(H_2)=5\times 10^5$ cm $^{-3}$.

determined by García-Burillo et al. (2001), $X(SiO)\sim 1\times 10^{-10}$, when compared with the SiO abundances, $\sim 10^{-8}$ – 10^{-6} , found in the shocks associated with galactic star forming regions (Martín-Pintado et al. 1992, Bachiller et al. 2001). In the case of H_2CO and CH_3OH we cannot do a detailed analysis because their lines are blended with other species.

5. Chemical model

We used the Meudon PDR code 1.4.4 (Le Petit et al. 2006) to model the chemistry in M 82. In our calculations, we assume that the ISM is composed of clouds bathed by an intense UV field. We simulate each cloud by a uniform plane-parallel layer illuminated from the two sides. This layer has constant density ($n=n(H)+2n(H_2)=4\times 10^5$ cm $^{-3}$) and the gas kinetic temperature is calculated by detailed heating and cooling balance. The adopted initial elemental abundances are the same as in Fuente et al. (2008). We run a grid of models varying the cloud size, UV field and cosmic rays ionization rate.

Our grid includes two values of the Draine field, 6×10^3 and 6×10^2 . The first value was determined by Fuente et al. (2005, 2006, 2008) from the CO^+ , HCO^+ and HOC^+ observations. The second value is considered to account for the possibility of regions with a lower UV field within the galaxy. To investigate the effect of the enhanced cosmic-ray flux on the chemistry, we have repeated our model calculations with $\zeta=5\times 10^{-17}$ and 5×10^{-15} s $^{-1}$. The first value corresponds to the cosmic rays ionization rate in the molecular clouds of our Galaxy (Indriolo et al. 2014). The second is the value estimated by Suchkov et al. (1993) to account for the physical conditions of the molecular gas in M 82. We are aware that X-rays are intense and could also play an important role in the chemistry (Fuente et al. 2008, Spaans & Meijerink 2007). Our code does not include the X-rays in the chemical calculations. We investigate the effect that X-rays could have on the chemistry by increasing the cosmic rays ionization rate to 5×10^{-14} s $^{-1}$. To increase the cosmic rays ionization rate reproduces reasonably well the effect of X-rays on the molecular chemistry although cannot account for the ef-

fect on the molecular gas heating. Finally, in our simple model, the cloud size is given by the total cloud visual extinction. We considered five values: 5 mag, 10 mag, 20 mag, 50 mag and 100 mag.

In Fig. 10 and Table 4 we show the cloud average molecular abundances as a function of the different model parameters. The large dispersion in the values is not unexpected since all the parameters are varied by several orders of magnitude. The cloud average abundances of CN, N_2H^+ , CS and HCO^+ increase with the cosmic rays ionization rate. This increase is especially important in the case of N_2H^+ . While the abundances of the other species increase by a factor of a few, the abundance of N_2H^+ increases by two orders of magnitude between $\zeta=5\times 10^{-17}$ and 5×10^{-14} s $^{-1}$. Surprisingly, the N_2H^+ abundance is quite constant in the studied knots. This suggests that the chemical changes we observe are not related with variation in the X-rays flux. We cannot discard, however, that variations in the UV field and cloud sizes could balance to keep the N_2H^+ abundance constant in spite of the variation of the X-rays flux (Strickland & Heckman 2007).

The cloud size is the parameter that has the largest impact on the results of our model. N_2H^+ has a negligible abundance in clouds with $A_V<10$ mag and abundances varying between 10^{-10} and 10^{-9} for larger clouds. This corroborates our assumption that this species is an excellent tracer of the UV-protected molecular gas. The $[CN]/[N_2H^+]$ ratio is a good measure of the cloud size in the case of one single cloud component. Fuente et al. (2008) proposed the existence of two cloud components towards E1: most of the mass, $\sim 87\%$, is locked in small clouds of $A_V\sim 5$ mag and the rest is forming $A_V>50$ mag clouds. In this case, the $[CN]/[N_2H^+]$ ratio would depend on both, the fraction of each cloud component and the assumed size for the large clouds.

The cloud average CS abundance is quite constant for sizes between ~ 5 and ~ 20 mag but increases by almost one order of magnitude for larger sizes. The large values of the CS abundance in the 50 mag clouds are not reliable. The CS abundance is very dependent on the assumed elemental sulphur abundance. Our gas phase models does not consider the adsorption of molecules on the grain surfaces. Within our galaxy, the sulphur abundance measured in PDRs is a factor >4 lower than the solar value, suggesting that significant sulphur depletion occurs even in highly irradiated environments (see Goicoechea et al. 2006). Moreover, our model assumes the solar value for the sulphur elemental abundance, 1.8×10^{-5} , that could greatly differ from that in M 82 (Umeda et al. 2002, Origlia et al. 2004). Therefore, we do not consider that the values of the CS abundance predicted by our model are reliable.

The $[CN]/[N_2H^+]$ ratio is a sensitive tracer of the cloud size for sizes <50 mag. Other parameters like the incident UV field and the cosmic rays ionization rate could also affect the predicted $[CN]/[N_2H^+]$ ratio. As expected, the $[CN]/[N_2H^+]$ ratio increases for higher UV fluxes, especially for small clouds. On the contrary, the $[CN]/[N_2H^+]$ ratio decreases with the cosmic rays ionization rate because of the increase of the N_2H^+ abundance. In the following, we discuss the cloud distribution in M 82 on basis of the $[CN]/[N_2H^+]$ ratio. We use our a priori knowledge of the galaxy to constrain the chemical models. We discuss the results for one- and two-component models.

In Fig. 11, we plot the $[CN]/[N_2H^+]$ abundance ratio as a function of the cloud size for Draine fields of 6×10^3 (high-UV) and 6×10^2 (low-UV). We adopt the value derived by Suchkov et al. (1993) for the cosmic rays ionization rate because it is the most likely. GP4 is the position with the highest value of the $[CN]/[N_2H^+]$ ratio and also the emission peak of the $H(41)\alpha$

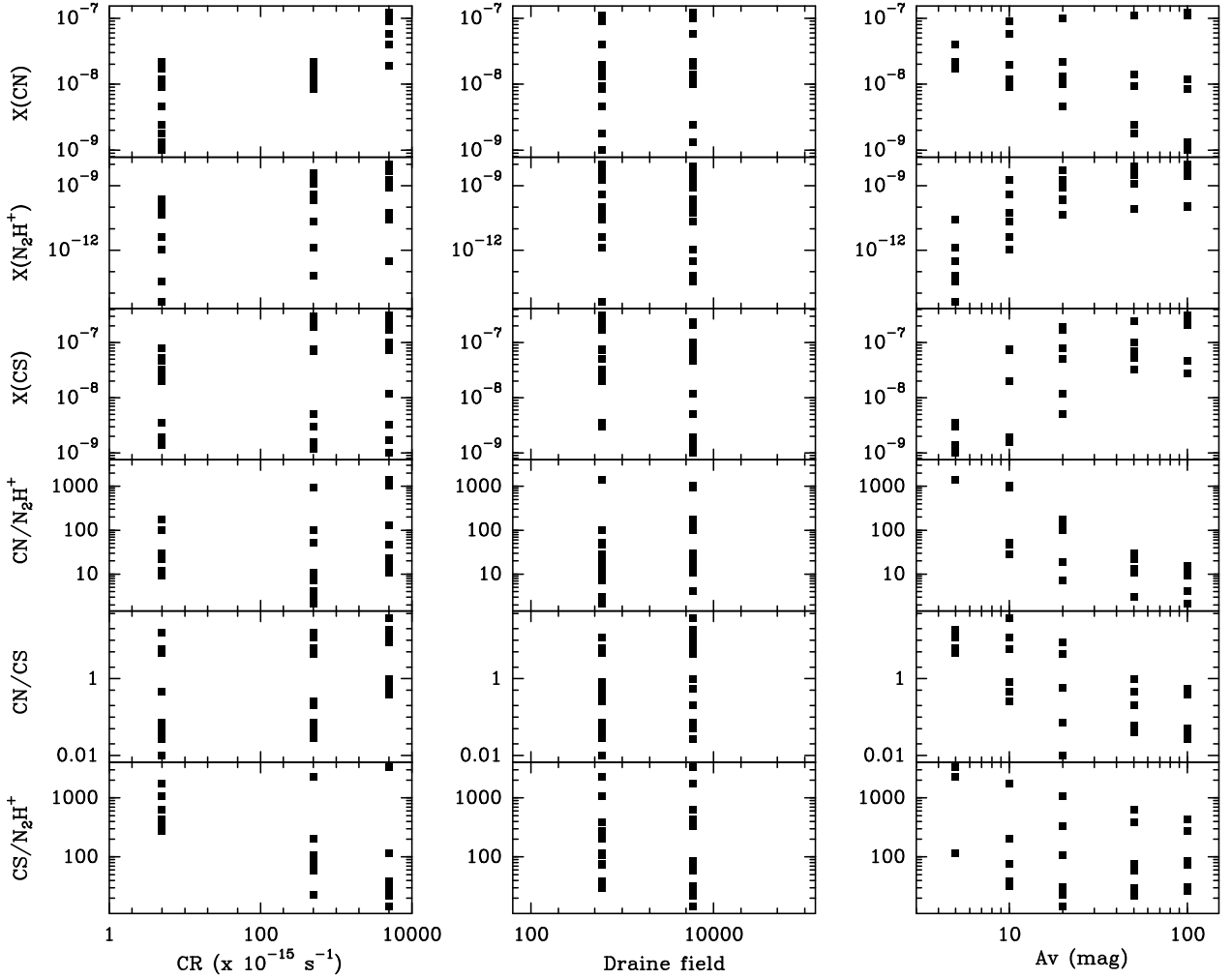


Fig. 10. Model predictions as a function of the cosmic ray ionization rate, Draine field and cloud size. Model parameters and results are shown in Table 4.

line. It is reasonable to think that high-UV models, in red lines in Fig. 11, are more adequate to account for the molecular abundances at this position. One single cloud component with sizes of ~ 22 mag could explain the observed $[\text{CN}]/[\text{N}_2\text{H}^+]$ ratio of ~ 80 . Lower $[\text{CN}]/[\text{N}_2\text{H}^+]$ ratios, ~ 30 , are measured towards the positions GP1 and GP6. Although less intense, these knots are also associated with peaks in the $\text{H}(41)\alpha$ line emission which proves the presence of energetic UV photons capable to ionize the atomic hydrogen (see Fig. A.3). Assuming the high-UV case, the lower $[\text{CN}]/[\text{N}_2\text{H}^+]$ ratio can be explained by the existence of a population of larger clouds, ~ 30 mag (see Fig. 11). The existence of larger clouds is also consistent with the lower kinetic temperatures and higher densities measured by Weiss et al. (2001b) and the detection of complex molecules at these positions. Low values of the $[\text{CN}]/[\text{N}_2\text{H}^+]$ ratio, ~ 20 – 30 , are also observed towards the SS2 and SS3 points placed in the molecular supershell. Since there is a lack of $\text{H}(41)\alpha$ emission towards these positions, we used the low-UV field models to interpret the $[\text{CN}]/[\text{N}_2\text{H}^+]$ ratio and obtained that the molecular emission could come from translucent clouds of ~ 14 mag.

The variation of the average cloud size we conclude from our one-component model is compatible with the results of Fuente et al. (2008) who interpreted the abundances in E1 in a two-component scenario. We can use a two-component model to explain our observations. In this case, the CN emission

would come from the small (with $A_v \sim 5$ mag) and large (with $A_v \sim 50$ mag) molecular clouds while the N_2H^+ emission would come only from large molecular clouds. Fuente et al. (2008) estimated that only $\sim 13\%$ of the molecular gas is forming large molecular clouds in E1. Assuming the same fraction at all positions, the $[\text{CN}]/[\text{N}_2\text{H}^+]$ ratio in the large cloud component would be about 0.13 times the observed one, i.e. ~ 10 in GP4, ~ 4 in GP1 and ~ 3 in SS3, i.e., we would have clouds of >50 mag in the three positions, with the largest ones, ~ 100 mag, towards GP1. Summarizing, both, the one and two-components models, come to the conclusion that the highest concentration of UV-protected molecular gas is found towards the x1 orbits. The detection of complex molecules is better understood in terms of two populations of clouds with a small fraction of the gas, $\sim 13\%$, locked in giant molecular clouds where the gas is UV protected and can form large molecules.

Of course, the two models are very simple and have to be understood as a guide to interpret the molecular chemistry in this starburst galaxy. As commented above, our model neglects the surface chemistry and X-rays effects that could be important for some species (see discussion above). Moreover our gas phase model assumes steady-state chemistry. The characteristic time for PDR chemistry is $\tau \sim 1/(\kappa_d G_0)$, where κ_d is the photodissociation rate in s^{-1} and G_0 is the incident UV field in Habing units. The value of κ_d depends on the extinction from the illuminat-

ing source as $\kappa_d \sim \kappa_0 \times \exp(-b A_v)$. Assuming a typical value of $\kappa_0 = 10^{-9} \text{ s}^{-1}$, $b = 1.8$ and the incident mean UV interstellar field in M 82, $G_0 = 10^4$ Habing fields, the characteristic time is > 10 Myr for $A_v > 2.5$ mag. This means that if the last starburst episode took place about ~ 5 – 10 Myr ago, the chemistry might be out of equilibrium in the clouds interior. Our steady-state scenario is therefore only adequate for the cloud surfaces and small clouds. The shortcoming of time-dependent models is that depend on the initial conditions and require of a more sophisticated analysis that is beyond the scope of this paper. Subsequent improvement of our current interpretation would require to couple the star formation history in this galaxy with a time-dependent PDR code including surface chemistry (Bayet et al. 2009, Viti et al. 2014, Bisbas et al. 2012).

For all species, the estimated fractional abundances in M 82 are lower than those predicted by our gas-phase model. Absolute fractional abundances are difficult to compare with models because of the large uncertainty in the total molecular gas column density. Weiss et al. (2001b) derived the total molecular gas column densities in M 82 using different methods: LVG calculations, Local Thermodynamic Equilibrium (LTE) solution and the standard X_{CO} conversion factor, and their results agree within a factor ~ 3 – 4 . In this paper, we derived the molecular column density towards the different points using the C^{18}O data and assuming the CO abundance derived by Weiss et al. (2001b), $X(\text{CO}) = 5 \times 10^{-5}$. We would like to note that this value is already lower than the value predicted by our model for large clouds in which essentially all the carbon is in CO with an abundance of $\sim 1.3 \times 10^{-4}$. Therefore our fractional abundances are accurate within a factor of 4–10 and consequently, roughly consistent with model predictions.

6. PDR and shock chemistry in M 82

M 82 has been subject of successive starburst episodes in the last ~ 200 Gyr. The most recent (~ 5 Myr) took place throughout the central regions of M 82 and was particularly intense in the $x2$ orbits and along the stellar bar. The negative feedback effects from this starburst activity is determining the existence and duration of future starburst episodes. We have carried out a chemical study of the molecular gas at scales of ~ 100 pc in order to investigate the feedback effects and the future star formation activity of the galaxy.

Our main result is that the chemistry of the molecular gas is determined by the intense UV radiation produced by the massive stars. There is a systematic variation of the studied molecular abundance ratios with the intensity of the $\text{H}(41)\alpha$ emission that corroborates that the whole nucleus (~ 650 pc), down to scales of ~ 100 pc, behaves like a giant PDR. Within this PDR, we have chemical variations due to changes in the local UV field and in the structure of the molecular clouds. There are three well differentiated regions:

- The inner $x2$ bar orbits that are associated with the most recent starburst and where the PDR tracers present their peak abundances. The detection of N_2H^+ in these regions proves that molecular clouds of > 20 mag are present and therefore, the molecular gas reservoir to form new stars is not exhausted.
- The outer $x1$ bar orbits where most the UV-protected molecular gas is located. The detection of $\text{H}(41)\alpha$ shows that massive stars have already been formed in these clouds.
- The molecular supershell associated with the supernova remnant SN 41.9+58. There are no signs of massive star forma-

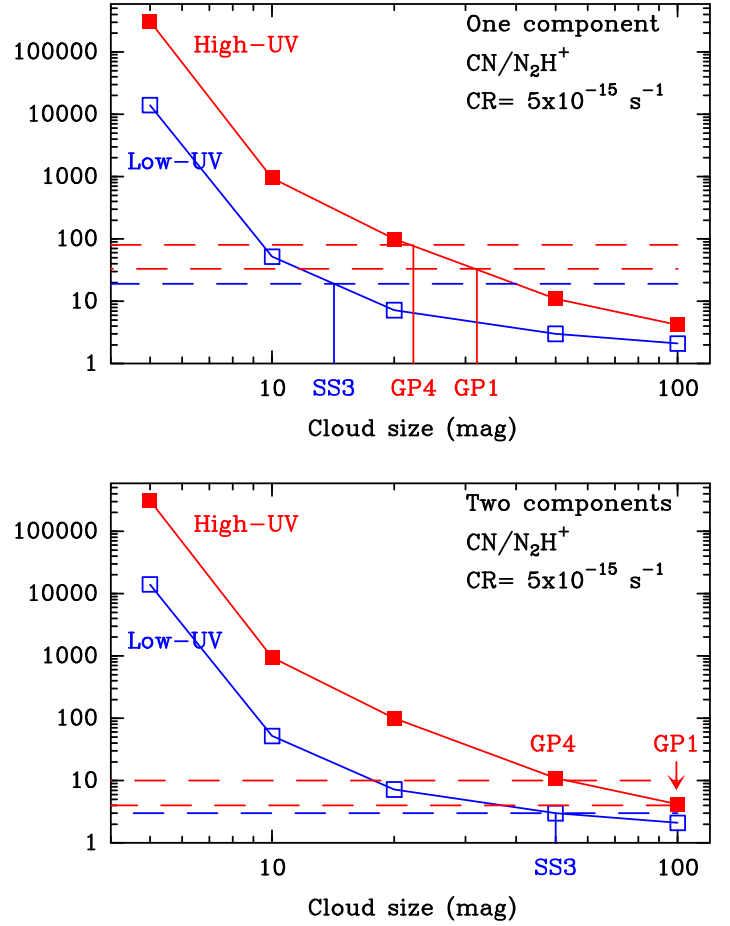


Fig. 11. $[\text{CN}]/[\text{N}_2\text{H}^+]$ abundance ratio as a function of the cloud size for models with $\text{CR} = 5 \times 10^{-15} \text{ s}^{-1}$ and Draine fields of 6×10^3 (red line) and $\times 10^3$ (blue line). **Top** Cloud sizes in the one-component model. **Bottom** Sizes of the large cloud component in the two-component model (see text). The values and errors for GP1, GP4 and SS3 are indicated.

tion activity in the southern part of this super-shell although there are intense N_2H^+ knots that could be sites for future star formation.

The detection of a ~ 500 pc molecular gas chimney and a super-shell in SiO indicates the occurrence of large-scale shocks in the disk-halo interface (García-Burillo et al. 2001). We remind that the supershell is related with the supernova explosion SN 41.9+58 that is launching ionized gas out of the galaxy plane. However, our data do not present any evidence of possible shock chemistry. This suggests that only a small fraction of the dense molecular gas is affected by shocks, which is also consistent with the low SiO abundance determined by García-Burillo et al. (2001), $X(\text{SiO}) \sim 1 \times 10^{-10}$, when compared with the SiO abundances, $\sim 10^{-8}$ – 10^{-6} , found in the shocks associated with galactic star forming regions (Martín-Pintado et al. 1992, Bachiller et al. 2001). Higher spatial resolution observations are required to detect the layer of molecular gas around the supershell whose chemistry is dominated by shocks. This is also consistent with the moderate fraction of dense molecular gas ($\sim 2\%$) that Salas et al. (2014) detected in the halo, in contrast with $\sim 25\%$ found by Walter et al. (2002) on basis of CO observations. Most of the expelled gas presents moderate densities and is not detected in dense molecular tracers.

Table 4. Chemical models¹

Model	CR ($\times 10^{-17}$)	Cloud size (mag)	Draine field	X(CN)	X(N ₂ H ⁺)	X(CS)	[CN]/[N ₂ H ⁺]	[CN]/[CS]	[CS]/[N ₂ H ⁺]
High-UV									
1	5000	100	6e3	1.2e-7	8.0e-9	2.1e-7	15	0.56	27
2	500	100	6e3	1.2e-8	2.8e-9	2.4e-7	4.2	0.05	85
3	5	100	6e3	1.3e-9	1.1e-10	4.7e-8	12	0.03	439
4	5000	50	6e3	1.1e-7	4.6e-9	1.0e-7	23	1.0	22
5	500	50	6e3	1.4e-8	1.2e-9	7.0e-8	11	0.2	58
6	5	50	6e3	2.4e-9	8.1e-11	5.2e-8	29	0.05	641
7	5000	20	6e3	1.0e-7	8.3e-10	1.2e-8	130	9.0	14
8	500	20	6e3	2.2e-8	2.2e-10	5.0e-9	100	4.4	22
9	5	20	6e3	1.0e-8	2.4e-10	8.0e-8	2173	0.07	333
10	5000	10	6e3	5.7e-8	5.3e-11	1.7e-9	1055	38	32
11	500	10	6e3	2.0e-8	2.1e-11	1.6e-9	952	12	76
12	5	10	6e3	1.2e-8	1.1e-12	1.9e-9	1.0e4	6	1727
13	5000	5	6e3	1.9e-8	3.0e-13	1.0e-9	6.4e4	19	3333
14	500	5	6e3	2.0e-8	6.4e-14	1.2e-9	3.1e5	16	18750
15	5	5	6e3	2.2e-8	3.6e-14	1.4e-9	6.1e5	16	38889
Low-UV									
16	5000	100	6e2	1.1e-7	1.0e-8	3.1e-7	11	0.38	30
17	500	100	6e2	8.6e-9	4.0e-9	3.0e-7	2.1	0.03	74
18	5	100	6e2	9.9e-10	1.0e-10	2.8e-8	9.4	0.03	270
19	5000	50	6e2	1.1e-7	8.2e-9	2.4e-7	13	0.45	29
20	500	50	6e2	9.4e-9	3.2e-9	2.4e-7	3	0.04	75
21	5	50	6e2	1.8e-9	8.4e-11	3.2e-8	122	0.06	380
22	5000	20	6e2	1.0e-7	5.5e-9	1.7e-7	19	0.59	31
23	500	20	6e2	1.3e-8	1.8e-9	1.9e-7	7	0.07	105
24	5	20	6e2	4.6e-9	4.6e-11	5.0e-8	98	0.01	1086
25	5000	10	6e2	8.9e-8	1.9e-9	7.2e-8	47	0.81	37
26	500	10	6e2	2.0e-8	3.8e-10	7.6e-8	52	0.26	200
27	5	10	6e2	9.0e-9	4.3e-12	2.0e-8	28	0.45	4651
28	5000	5	6e2	4.0e-8	2.8e-11	3.2e-9	1428	12	114
29	500	5	6e2	1.8e-8	1.3e-12	3.0e-9	1.4e4	6	2307
30	5	5	6e2	1.7e-8	4.0e-15	3.6e-9	4.3e6	5	9E5

¹ Notation: 6e3 = 6×10^3

Summarizing, we present a comprehensive chemical study of the molecular gas in the starburst galaxy M 82 using high spatial resolution (60–100 pc) interferometric images. Our chemical study shows that the feedback effects are strong in this evolved starburst. In fact, the whole nucleus presents a PDR-like chemistry which suggests that UV radiation is driven by the subsequent evolution of the ISM. Even though, the detection of N₂H⁺ proves the existence of dense molecular gas enclosed in clouds of $A_V > 20$ mag that could form new stars. The main reservoir of the dense molecular gas is located in the outer $x1$ orbits that might be the preferred site for a new generation of stars proceeding with the inside-outside scenario.

Acknowledgements. AF thanks the Spanish MINECO for funding support from grants CSD2009-00038 and AYA2012-32032. SGB acknowledges support from Spanish grants CSD2009-00038, AYA2010-15169, AYA2012-32295, AYA2013-42227-P and from the Junta de Andalucía through TIC-114 and the Excellence Project P08-TIC-03531. PP acknowledges financial support from the Centre National d'Etudes Spatiales (CNES).

References

- Achtermann, J. M., & Lacy, J. H. 1995, *ApJ*, 439, 163
 Aladro, R., Martín, S., Martín-Pintado, J., et al. 2011, *A&A*, 535, AA84
 Bachiller, R., Fuente, A., Bujarrabal, V., et al. 1997, *A&A*, 319, 235
 Bachiller, R., Pérez Gutiérrez, M., Kumar, M. S. N., & Tafalla, M. 2001, *A&A*, 372, 899
 Bayet, E., Viti, S., Williams, D. A., Rawlings, J. M. C., & Bell, T. 2009, *ApJ*, 696, 1466
 Bisbas, T. G., Bell, T. A., Viti, S., Yates, J., & Barlow, M. J. 2012, *MNRAS*, 427, 2100
 Boger, G. I., & Sternberg, A. 2005, *ApJ*, 632, 302
 Bregman, J. N., Schulman, E., & Tomisaka, K. 1995, *ApJ*, 439, 155
 Cernicharo, J. 2012, in *Proceedings of the European Conference on Laboratory Astrophysics*, Eur. Astron. Soc. Publ. Ser., eds. C. Stehl, C. Joblin, & L. d'Hendecourt
 Cuadrado, S., Goicoechea, J. R., Pilleri, P., et al. 2014, arXiv:1412.0417
 Förster Schreiber, N. M., Genzel, R., Lutz, D., & Sternberg, A. 2003, *ApJ*, 599, 193
 Fuente, A., Martín-Pintado, J., Cernicharo, J., & Bachiller, R. 1993, *A&A*, 276, 473
 Fuente, A., Martín-Pintado, J., & Gaume, R. 1995, *ApJ*, 442, L33
 Fuente, A., Rodríguez-Franco, A., & Martín-Pintado, J. 1996, *A&A*, 312, 599

Appendix A: Tables and Figures

- Fuente, A., Rodríguez-Franco, A., García-Burillo, S., Martín-Pintado, J., & Black, J. H. 2003, *A&A*, 406, 899
- Fuente, A., García-Burillo, S., Gerin, M., et al. 2005, *ESA Special Publication*, 577, 281
- Fuente, A., García-Burillo, S., Gerin, M., et al. 2006, *ApJ*, 641, L105
- Fuente, A., García-Burillo, S., Usero, A., et al. 2008, *A&A*, 492, 675
- García-Burillo, S., Martín-Pintado, J., Fuente, A., & Neri, R. 2000, *A&A*, 355, 499
- García-Burillo, S., Martín-Pintado, J., Fuente, A., & Neri, R. 2001, *ApJ*, 563, L27
- García-Burillo, S., Martín-Pintado, J., Fuente, A., Usero, A., & Neri, R. 2002, *ApJ*, 575, L55
- Goicoechea, J. R., Pety, J., Gerin, M., et al. 2006, *A&A*, 456, 565
- Greve, A., Wills, K. A., Neininger, N., & Pedlar, A. 2002, *A&A*, 383, 56
- Greve, A. 2011, *A&A*, 529, AA51
- Guzmán, V. V., Pety, J., Gratier, P., et al. 2014, *arXiv:1404.7798*
- Guzmán, V. V., Goicoechea, J. R., Pety, J., et al. 2013, *A&A*, 560, AA73
- Indriolo, N., Neufeld, D. A., Gerin, M., et al. 2014, *arXiv:1412.1106*
- Joy, M., Lester, D. F., & Harvey, P. M. 1987, *ApJ*, 319, 314
- Kronberg, P. P., Biermann, P., & Schwab, F. R. 1981, *ApJ*, 246, 751
- Le Petit, F., Nehmé, C., Le Boulrot, J., & Roueff, E. 2006, *ApJS*, 164, 506
- Lester, D. F., Gaffney, N., Carr, J. S., & Joy, M. 1990, *ApJ*, 352, 544
- Li, S., de Grijis, R., Anders, P., & Li, C. 2015, *ApJS*, 216, 6
- Liszt, H., & Lucas, R. 2001, *A&A*, 370, 576
- Mao, R. Q., Henkel, C., Schulz, A., et al. 2000, *A&A*, 358, 433
- Martín, S., Martín-Pintado, J., & Mauersberger, R. 2006, *A&A*, 450, L13
- Martín-Pintado, J., Bachiller, R., & Fuente, A. 1992, *A&A*, 254, 315
- Murray, N. 2011, *ApJ*, 729, 133
- Neininger, N., Guelin, M., Klein, U., García-Burillo, S., & Wielebinski, R. 1998, *A&A*, 339, 737
- Origlia, L., Ranalli, P., Comastri, A., & Maiolino, R. 2004, *ApJ*, 606, 862
- Pety, J., Teyssier, D., Fossé, D., et al. 2005, *A&A*, 435, 885
- Pilleri, P., Treviño-Morales, S., Fuente, A., et al. 2013, *A&A*, 554, AA87
- Salas, P., Galaz, G., Salter, D., et al. 2014, *ApJ*, 797, 134
- Shen, J., & Lo, K. Y. 1995, *ApJ*, 445, L99
- Shopbell, P. L., & Bland-Hawthorn, J. 1998, *ApJ*, 493, 129
- Spaans, M., & Meijerink, R. 2007, *ApJ*, 664, L23
- Strickland, D. K., & Heckman, T. M. 2007, *ApJ*, 658, 258
- Suchkov, A., Allen, R. J., & Heckman, T. M. 1993, *ApJ*, 413, 542
- Umeda, H., Nomoto, K., Tsuru, T. G., & Matsumoto, H. 2002, *ApJ*, 578, 855
- Usero, A., García-Burillo, S., Martín-Pintado, J., Fuente, A., & Neri, R. 2006, *A&A*, 448, 457
- Viti, S., García-Burillo, S., Fuente, A., et al. 2014, *A&A*, 570, AA28
- Walter, F., Weiss, A., & Scoville, N. 2002, *ApJ*, 580, L21
- Weiβ, A., Walter, F., Neininger, N., & Klein, U. 1999, *A&A*, 345, L23
- Weiβ, A., Neininger, N., Henkel, C., Stutzki, J., & Klein, U. 2001a, *ApJ*, 554, L143
- Weiβ, A., Neininger, N., Hüttemeister, S., & Klein, U. 2001b, *A&A*, 365, 571
- Wills, K. A., Redman, M. P., Muxlow, T. W. B., & Pedlar, A. 1999, *MNRAS*, 309, 395
- Wills, K. A., Das, M., Pedlar, A., Muxlow, T. W. B., & Robinson, T. G. 2000, *MNRAS*, 316, 33

Table A.1. Gaussians parameters to the observed spectra¹

E1 (+14'', +5'')						
Line		Freq(GHz)	I(K km s ⁻¹)	v_{lsr} (km s ⁻¹)	Δv (km s ⁻¹)	T_{MB} (K)
CN	1 \rightarrow 0	113.491	64.15 (0.56)	316.26 (0.33)	75.73 (0.77)	0.79
H ¹³ CO ⁺	1 \rightarrow 0	86.754	4.52 (0.67)	324.66 (5.02)	69.39 (12.4)	0.06
H	41 α	92.034	5.42 (0.19)	320.48 (1.21)	70.79 (2.89)	0.07
CH ₃ CN	5 $_k \rightarrow$ 4 $_k^*$	91.987	2.43 (0.20)	328.58 (3.13)	74.26 (6.62)	0.03
N ₂ H ⁺	1 \rightarrow 0	93.173	6.98 (0.17)	321.42 (0.73)	60.23 (1.57)	0.11
C ¹⁸ O	1 \rightarrow 0	109.782	22.74 (0.62)	324.40 (0.93)	69.58 (2.18)	0.31
C ₃ H ₂	3 \rightarrow 2	145.089	9.90 (0.24)	315.23 (0.75)	63.77 (1.69)	0.14
H ₂ CO	2 _{0,2} \rightarrow 1 _{0,1}	145.603	8.45 (0.20)	321.30 (0.67)	56.90 (1.58)	0.14
HC ₃ N	16 \rightarrow 15	145.561	4.35 (0.17)	330.32 (0.90)	43.12 (1.96)	0.09
CS	3 \rightarrow 2	145.760	31.84 (0.37)	322.56 (0.32)	55.63 (0.71)	0.54
E2 (+5'', +2'')						
Line		Freq(GHz)	I(K km s ⁻¹)	v_{lsr} (km s ⁻¹)	Δv (km s ⁻¹)	T_{MB} (K)
CN	1 \rightarrow 0	113.491	56.09 (0.53)	249.23 (0.35)	79.56 (0.92)	0.66
			4.83 (0.30)	330.76 (0.78)	26.26 (1.70)	0.17
H ¹³ CO ⁺	1 \rightarrow 0	86.754	2.19 (0.30)	258.66 (4.28)	57.14 (7.48)	0.03
H	41 α	92.034	7.25 (0.24)	278.04 (1.89)	121.01 (5.46)	0.06
CH ₃ CN	5 $_k \rightarrow$ 4 $_k^*$	91.987	1.35 (0.20)	284.18 (5.79)	85.36 (13.7)	0.01
N ₂ H ⁺	1 \rightarrow 0	93.173	3.74 (0.15)	255.80 (1.08)	58.24 (2.89)	0.06
C ¹⁸ O	1 \rightarrow 0	109.782	9.22 (0.65)	259.28 (1.78)	53.14 (4.66)	0.16
C ₃ H ₂	3 \rightarrow 2	145.089	4.95 (0.17)	245.88 (0.88)	53.58 (2.13)	0.09
			0.57 (0.12)	311.92 (2.90)	26.65 (5.71)	0.02
H ₂ CO	2 _{0,2} \rightarrow 1 _{0,1}	145.603	4.34 (0.16)	256.14 (0.77)	45.57 (1.98)	0.09
HC ₃ N+H ₂ CO ²		145.561	2.85 (0.17)	253.33 (1.48)	53.47 (3.90)	0.05
CS	3 \rightarrow 2	146.969	16.83 (0.15)	258.63 (0.20)	46.79 (0.53)	0.34
			1.43 (0.11)	329.47 (0.94)	25.13 (2.28)	0.05
W2 (-5'', -2'')						
Line		Freq(GHz)	I(K km s ⁻¹)	v_{lsr} (km s ⁻¹)	Δv (km s ⁻¹)	T_{MB} (K)
CN	1 \rightarrow 0	113.491	10.65 (0.82)	95.78 (0.37)	25.788 (1.18)	0.39
			56.67 (0.59)	99.31 (0.62)	92.166 (2.18)	0.58
			20.75 (0.54)	156.73 (1.09)	68.352 (1.92)	0.28
H ¹³ CO ⁺	1 \rightarrow 0	86.754	2.86 (0.50)	115.70 (10.6)	111.91 (18.2)	0.02
H	41 α	92.034	10.75 (0.29)	103.65 (0.59)	81.50 (1.71)	0.12
			8.87 (0.39)	172.86 (7.51)	352.24 (18.08)	0.02
CH ₃ CN	5 $_k \rightarrow$ 4 $_k^*$	91.987				<0.015
N ₂ H ⁺	1 \rightarrow 0	93.173	3.85 (0.13)	93.13 (6.28)	48.56 (6.28)	0.07
			1.47 (0.13)	145.67 (6.28)	35.74 (6.28)	0.04
			0.91 (0.13)	183.60 (6.28)	30.43 (6.28)	0.03
C ¹⁸ O	1 \rightarrow 0	109.782	10.45 (0.60)	130.29 (3.30)	111.32 (7.20)	0.09
C ₃ H ₂	3 \rightarrow 2	145.089	4.72 (0.20)	89.20 (1.04)	55.84 (2.74)	0.08
			2.98 (0.21)	162.01 (0.31)	64.91 (4.64)	0.04
H ₂ CO*	2 _{0,2} \rightarrow 1 _{0,1}	145.603	2.96 (0.25)	95.22 (0.90)	37.15 (2.58)	0.07
HC ₃ N+H ₂ CO ³		145.561	8.20 (0.70)	93.10 (3.30)	93.54 (10.92)	0.08
CS	3 \rightarrow 2	146.969	10.96 (2.52)	96.54 (3.24)	37.31 (4.49)	0.27
			7.77 (3.55)	136.99 (4.27)	42.03 (16.7)	0.17
			4.22 (1.47)	182.91 (4.92)	34.698.89)	0.11
W1 (-14'', -5'')						
Line		Freq(GHz)	I(K km s ⁻¹)	v_{lsr} (km s ⁻¹)	Δv (km s ⁻¹)	T_{MB} (K)
CN	1 \rightarrow 0	113.491	62.38 (0.58)	103.05 (0.36)	80.399 (0.87)	0.73
H ¹³ CO ⁺	1 \rightarrow 0	86.754	3.90 (0.57)	104.39 (5.51)	76.888 (13.54)	0.05
H	41 α	92.034	4.76 (0.18)	98.51 (1.52)	80.41 (3.65)	0.06
CH ₃ CN	5 $_k \rightarrow$ 4 $_k^*$	91.987	1.78 (0.17)	127.93 (3.60)	71.73 (7.26)	0.02
N ₂ H ⁺	1 \rightarrow 0	93.173	6.61 (0.16)	113.57 (0.74)	62.23 (1.81)	0.10
C ¹⁸ O	1 \rightarrow 0	109.782	24.90 (0.51)	118.46 (0.65)	63.32 (1.45)	0.37
C ₃ H ₂	3 \rightarrow 2	145.089	13.00 (0.72)	103.29 (1.55)	57.80 (3.92)	0.21
H ₂ CO	2 _{0,2} \rightarrow 1 _{0,1}	145.603	6.12 (0.51)	110.67 (1.18)	47.71 (2.57)	0.12
HC ₃ N	16 \rightarrow 15	145.561	3.66 (1.52)	100.41 (18.4)	93.16 (43.1)	0.04
CS	3 \rightarrow 2	145.760	29.52 (0.26)	116.01 (0.24)	54.22 (0.55)	0.51

¹The PdBI images have been convolved to the same angular resolution (5.9'' x 5.9''). *The k=0,1,2 and 3 components are blended. The velocity of the Gaussian fit is calculated relative to the frequency of the k=0 component, $\nu=91987$ MHz. ²The ~ 326 km s⁻¹ component of H₂CO overlap with the ~ 270 km s⁻¹ component of HC₃N. ³A possible ~ 180 km s⁻¹ component of H₂CO would overlap with the ~ 93 km s⁻¹ component of HC₃N.

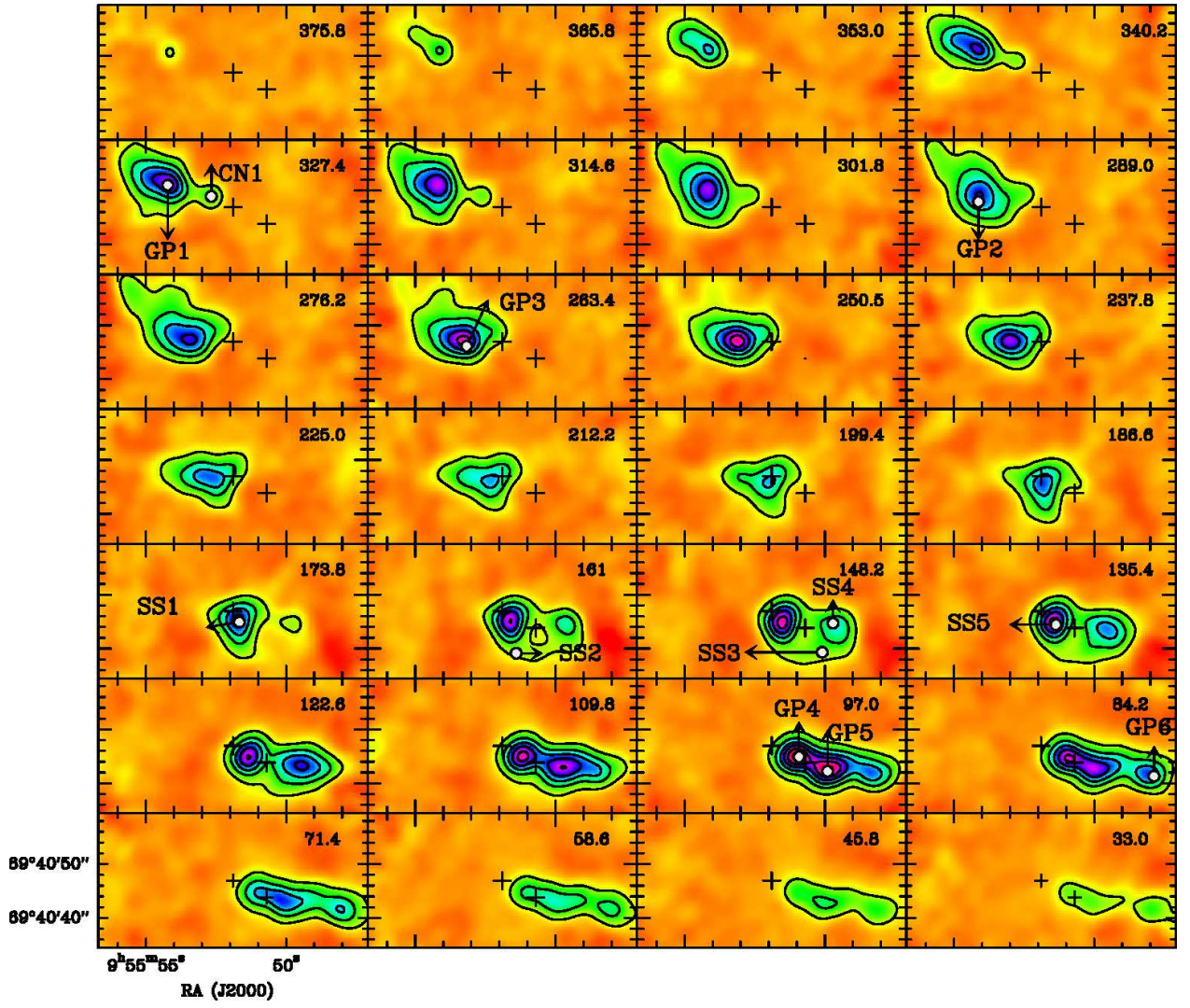


Fig. A.1. Spectral maps of the CN $1 \rightarrow 0$ line convolved to an angular resolution of $3.8''$. To increase the S/N ratio, the velocity resolution has been degraded to 12.8 km s^{-1} . The number in the right-upper corner indicates the central channel velocity. Contour levels are $0.17 (5\sigma)$ to 1.955 in steps of 0.255 K . Crosses indicate the dynamical center of the galaxy and the position of SN 41.9+58.

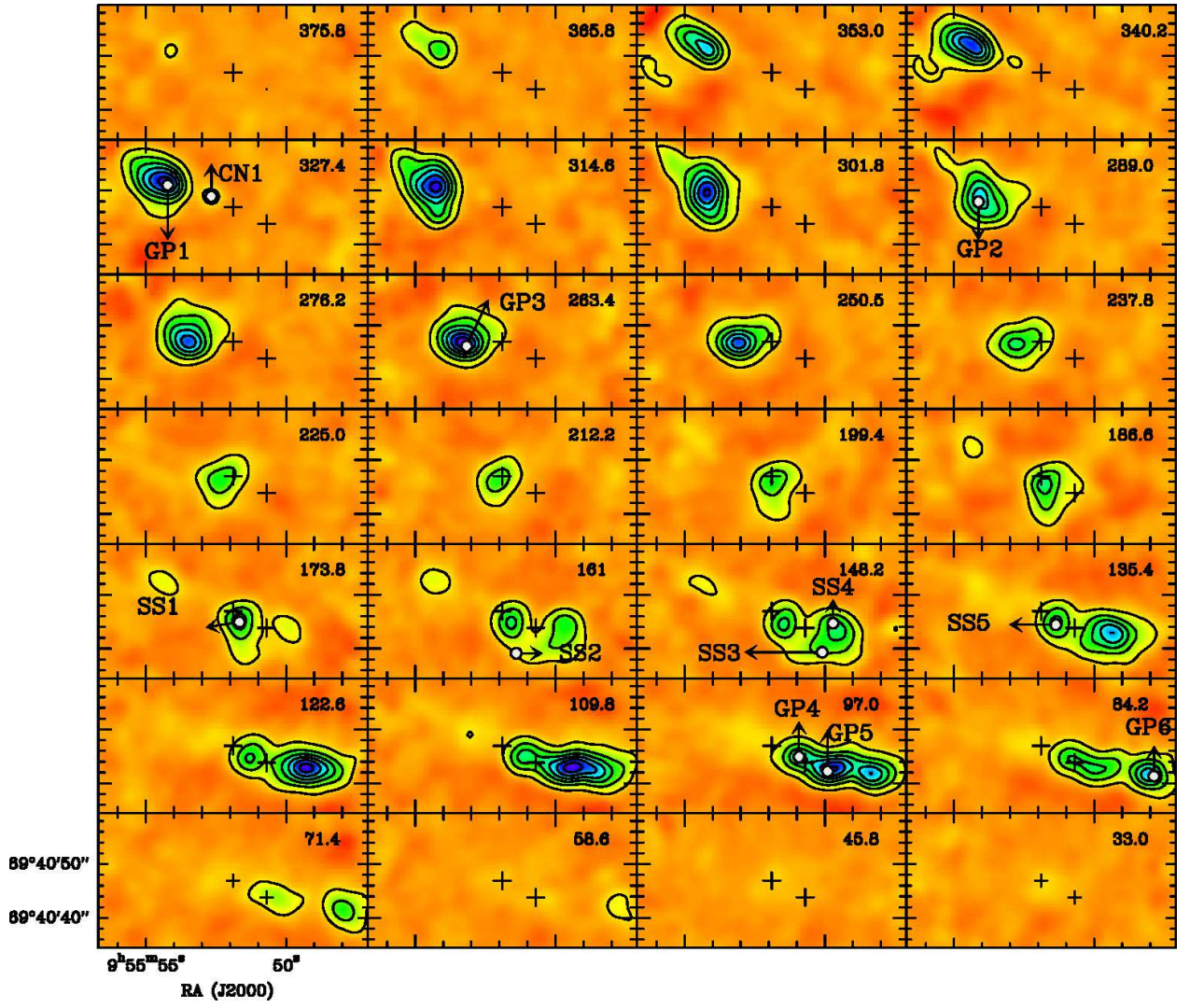


Fig. A.2. The same as Fig. A.1 for the CS 3 \rightarrow 2 line. Contour levels are 0.065 ($3\times\sigma$) to 1.495 in steps of 0.13 K. The eastern knot at velocities ~ 144 - 192 km s $^{-1}$ is due to the emission of the H(35) α line.

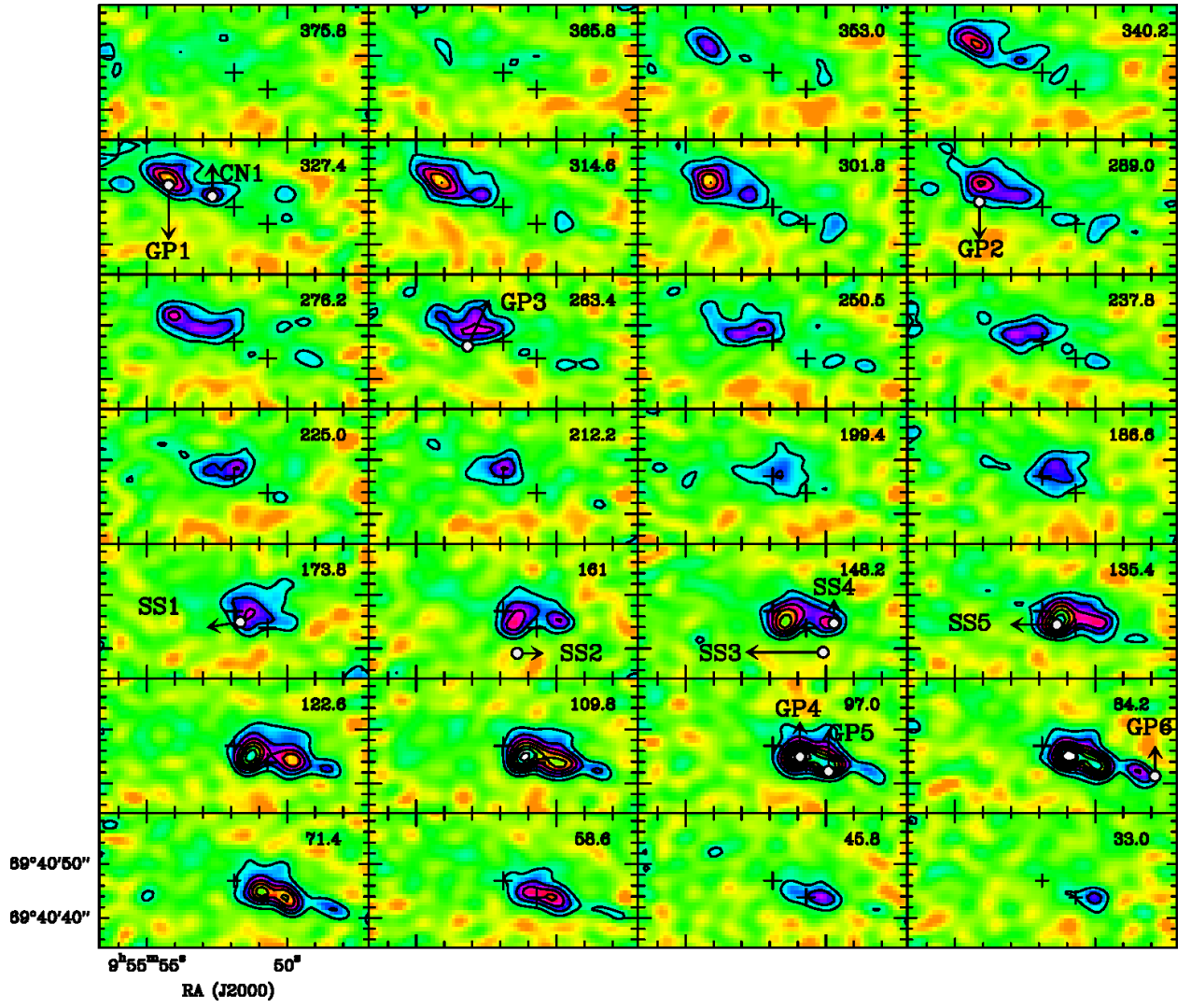


Fig. A.3. The same as Fig. A.1 for the H(41)α line. First contour and step are 0.028 K ($\sim 3\sigma$).